Numerical continuation and stability of nonlinear systems with distributed delays: Application to fluid-induced impacts of tubes in cross-flow

Roberto Alcorta, Benoît Prabel, Sébastien Baguet, Philippe Piteau

Author manuscript, published in "International Journal of Non-Linear Mechanics", Vol 161, 104667 (2024)
DOI: 10.1016/j.ijnonlinmec.2024.104667
The final publication is available at Elsevier via www.sciencedirect.com

Numerical continuation and stability of nonlinear systems with distributed delays: application to fluid-induced impacts of tubes in cross-flow

Roberto Alcorta[a,*], Benoit Prabel[b], Sebastien Baguet[a], Philipe Piteau[b]

[a] *INSA Lyon, CNRS, LaMCoS, UMR5259, 69621 Villeurbanne, France*
[b] *Université Paris-Saclay, CEA, Service d'Études Mécaniques et Thermiques, 91191, Gif-sur-Yvette, France*

Abstract

Fluid-elastic instability is the main source of concern during the design of heat-exchanger tube bundles. The associated research has focused on the understanding of the physical mechanisms behind this phenomenon and the establishing of models capable of predicting its onset; also some concomitant work has been done to establish post-instability behaviour and to prevent from excessive wear in possible sliding contacts. Moreover, the existing studies make use of time-integration methods alone for this purpose, through which it is difficult to get a comprehensive insight of global dynamics. Continuation methods, which give access to unstable branches and precise bifurcation information, are a precious tool to unfold the attainable dynamic regimes. In this paper, the parametric behaviour of two representative systems under cross-flow excitation is explored through pseudo arc-length continuation with mean flow velocity as a main driving parameter, wherein the nonlinear modal equations of motion are solved by harmonic balance at each step. As the quasi-unsteady model used for fluid-elastic coupling introduces convolution integrals, this approach is quite natural and we show that, despite some difficulties regarding the treatment of stiff intermittent contacts, it allows for a thorough exploration of the system's response. For the first case -a benchmark model-, increasingly complex dynamics arise as more modes are kept in the truncated modal basis, which is due to a series of modal interactions as the impacts distribute mechanical energy from the linearly-unstable first mode to the higher ones. This can be anticipated by studying the nonlinear normal modes of the system, as they expose the allowed internal resonances. In the second case, consisting of a realistic heat-exchanger tube configuration, a similar pattern is observed.

Keywords: Fluid-elastic instability, nonlinear vibrations, distributed delays, harmonic balance, impact

1. Introduction

Among the different mechanisms responsible for flow-induced vibrations of heat-exchanger tube bundles, fluid-elastic instability is certainly the most critical one [1]. In the broadest sense, this term denotes the destabilization of one or more tubes' static equilibrium position due to interactions with the flow as the velocity of the latter exceeds a certain threshold, leading to self-excited motions with exponentially-growing amplitudes. When this happens, displacements are limited only by nonlinear effects such as tube-support impacts, leading to premature failure by excessive wear. Behind this deceivingly simple description, however, lies an astoundingly complex physical process which has so-far eluded a full understanding. Indeed, the corresponding scientific literature is vast and spans six decades; comprehensive reviews include the works by Connors [2], Païdoussis [3, 4, 5, 6], Chen [7, 8], Pettigrew et al. [9], Price [10], Gelbe [11] and Sarpkaya [12], as well as the books by Axisa [1], Gibert [13] and Païdoussis et al. [14]. In the context of nuclear power plant steam-generator tube bundles, for instance, design guidelines are under constant revision and updating, with the publications by Sun et al. [15] and Taylor and Pettigrew [16] being recent examples. Despite the differences amongst the numerous proposed models, however, some salient features are nearly ubiquitous. In particular, this is true about the use of time-delayed terms as a source for instability, whether in discrete or continuous form.

*Corresponding author
Email address: roberto.alcorta@insa-lyon.fr (Roberto Alcorta)

On the other hand, the problem of predicting instability onset has received a great deal of attention, with some studies also focusing on the post-instability, nonlinear behaviour of tube bundles. the latter is an important subject, as it relates to off-design operation in which support gaps have widened due to misalignment or wear. In a series of papers, Borsoi and co-workers investigated different aspects of the dynamics of a 1-DOF model consisting of an autonomous oscillator destabilized by fluid-elastic forces, computed by the Granger and Païdoussis quasi-unsteady model with empirical coefficients obtained through active control [17]. In [18], for instance, the authors reported coexisting symmetric (two-sided impacts) and asymmetric (one-sided impacts) periodic cycles for certain values of flow velocity, in the case where turbulence was ignored. When turbulence was included, tube motions in phase were seen to be erratic but clearly stayed in the vicinity of said cycles. On the other hand, Prabel et al. [19] used the quasi-unsteady model to numerically simulate the response of a U-tube in cross-flow with a realistic velocity and density distribution. To this end, the two-phase flow was homogenized into an equivalent single-phase flow. The obtained results showed an increase in the complexity of the responses as the number of modes considered was increased. Lai et al. [20] used time-integration to numerically study the behaviour of a flexible, cantilever beam in a rigid, rotated-triangular grid under the action of a two-phase cross-flow. Fluid-elastic forces were computed through the Price and Païdoussis model [21] fitted with experimental data, and transitions from steady periodic to quasi-periodic and chaotic motions were observed for increasing flow velocity.

It should be clear that the combination of impacts with delayed forces leads to a particularly intricate and rich dynamical behaviour, thus calling for robust numerical methods to allow for thorough analysis. As the nature and number of solutions are clearly dependent on parameters -with the most important one being flow velocity-, numerical continuation methods seem to be ideally suited for the task. Indeed, some well-established continuation codes exist which are able to deal with general delay differential equations and their stability, such as DDE-BIFTOOL [22] and KNUT [23]. Both of these, however, make use of time-domain approaches to perform the required computations. Recently, the bifurcation analysis of time-delay systems within the framework of the COCO software [24] was proposed, although the particular implementation also relied on time-domain formulation of the problem. On the other hand, continuation based on the Harmonic Balance Method (HBM) [25, 26, 27] offers a convenient alternative, since the time-delay terms involved in fluid-elastic instability models can be readily expressed in the frequency domain without an increase in system size. Moreover, such an approach is aligned with current trends in engineering, where HBM is the method of choice to treat large-scale nonlinear models obtained by finite-element discretization in diverse contexts, including saturated electromagnetic systems [28] and aerospace structures with localized [29] and distributed [30] nonlinearities. However, to the authors' best knowledge, studies of this kind are currently absent from the literature. A possible explanation for this is the fact that, due to contacts, several of the tubes' vibration modes are excited at once, which renders periodic solutions rare -if at all existent- for an autonomous dynamical system [31]. This situation is to be contrasted to, e.g. studies on aeroelasticity [32, 33, 34], where the discrete models representing rigid-body motions are not issued from a (modal or otherwise) projection. In the present paper, we intends show that the study of periodic branches yields valuable insight into the nonlinear dynamics of fluid-elastically unstable tubes in cross-flow, and provide the means to do so efficiently with a frequency-domain continuation approach. To this end, a mathematical formulation of the problem is presented in Sect. 2. The proposed numerical approach is described in Sect 3., which includes a novel formulation of the Hill matrix for stability computation. The algorithms are tested on two systems in Sect. 4, with the first one being quasi-academic in nature and the second one being closer to the targeted industrial application.

2. A mathematical model for transverse vibrations of unstable tubes

2.1. Generalities

The tubes considered satisfy the hypotheses of Euler-Bernoulli beam theory, and thus can be aptly modelled by using 1D beam elements, constituting a mesh $\mathfrak{D} \subset \mathbb{R}^3$ which provides a spatial discretization for the geometry. Thus, letting $x \in [0, L]$ represent the curvilinear abscissa following the elastic axis of a tube with total length L, the

transverse[1] displacements $y(x,t)$ satisfy:

$$\rho_s S \frac{\partial^2 y}{\partial t^2} + \eta \frac{\partial y}{\partial t} + \frac{\partial^2}{\partial x^2}\left(EI\frac{\partial^2 y}{\partial x^2}\right) + f_f + f_t + \sum_{k=1}^{N_c} f_{c,k}\left(y,\dot{y}\right)\delta\left(x - x_{c,k}\right) = 0 \tag{1}$$

where the different force terms correspond to:

- $f_f(x,t)$: damping-controlled fluid-elastic coupling.
- $f_t(x,t)$: excitation by broadband turbulence.
- $f_{c,k}(y,\dot{y})$: reaction at contact points.

The above equation considers an arbitrary number N_c of contact points $x_{c,k}, k = 1, ..., N_c$ along the tube's span. In actual heat-exchanger systems, supports are practically rigid whereas tubes deformed elastically over the duration of contact. This is equivalent to considering a rigid tube and a compliant support, thus justifying the use of a penalty formulation to compute contact forces. Following [35], these are given by:

$$f_{c,k}(y,\dot{y}) = \begin{cases} k_c\left(y - g_k\right) + c_c\dot{y} & \text{if} \quad k_c\left(y - g_k\right) + c_c\dot{y} > 0 \quad \text{and} \quad y > g_k \\ k_c\left(y + g_k\right) + c_c\dot{y} & \text{if} \quad k_c\left(y + g_k\right) + c_c\dot{y} < 0 \quad \text{and} \quad y < -g_k \\ 0 & \text{else} \end{cases} \tag{2}$$

in which the cross-section ovalization stiffness, k_c, acts as a physical penalty coefficient. In the case of typical steam-generator tube arrays, this parameter is $O(10^6)$ N/m. Likewise, piecewise-linear damping has been introduced to account for potential energy losses [36], with $c_c = 0$ corresponding to perfectly elastic impacts. Finally, the size of the k-th gap is denoted g_k. In this paper we assume the tube's equilibrium position $y = 0$ to lie at the midpoint between both supports, although the model readily generalizes to asymmetric configurations. As our objective is to use continuation methods, it is convenient to approximate the piecewise-linear Eq. (2) by a smooth function, as follows:

$$f_{c,k}(y,\dot{y}) \approx k_c y + c_c\dot{y} + \frac{1}{2}\left[\sqrt{(k_c(y - g_k) + c_c\dot{y})^2 + 4k_c\eta} - \sqrt{(k_c(y + g_k) + c_c\dot{y})^2 + 4k_c\eta}\right] \tag{3}$$

where η is an adjustable parameter controlling the artificial smoothing of contact forces. One can readily verify that Eq. (3) reduces to (2) as $\eta \to 0$. This smoothing procedure is not unique, and the reader is referred to [37] for an exploration of different smooth approximations used in contact modelling. From a dynamics perspective, Eq. (3) with $\eta > 0$ is unable to capture non-smooth singularities such as the grazing bifurcation [38]. This aspect, however, is beyond the scope of the present paper. The function $f_{c,k}$ is represented in Fig. 1.

The term f_t is random by nature, and thus prevents the establishment of (periodic or otherwise) steady-state vibratory regimes. In what follows, it will be neglected under the assumption that fluctuations from turbulent fields introduce perturbations on the limit cycles of the system, without altering its underlying dynamics. This means that, for fixed parameter values, the number and nature of coexisting attractors is unchanged by turbulence. The authors make no claim regarding the universality of this assumption, which is quite a strong one and has been verified only a posteriori for the present case.

Finally, f_f is given by the *quasi-unsteady* (QU) model of Granger & Païdoussis [39], as follows:

$$f_f(x,t) = \frac{1}{2}\rho_f(x)V(x)D\left(C_D\dot{y} - \frac{V(x)^2}{D^2}\frac{\partial C_L}{\partial y}(\bar{h} * y)\right) \tag{4}$$

The first term in Eq. (4) represents added damping, whereas the second introduces a memory effect through convolution with the following kernel function, which represents an impulse:

$$\bar{h}(\tau) = \sum_{k=1}^{n_e} \alpha_k\delta_k e^{-\delta_k\frac{V_M}{D}\tau}\hat{H}(\tau) + \frac{D}{V(x)}\alpha_0\hat{\delta}(\tau) = \sum_{k=1}^{n_e}\bar{h}_k\hat{H}(\tau) + \bar{h}_0\hat{\delta}(\tau), \tag{5}$$

[1] It should be noted that the restriction made here to out-of-plane transverse vibrations is adopted solely for simplicity, since the generalization to arbitrary, three-dimensional motions is straightforward.

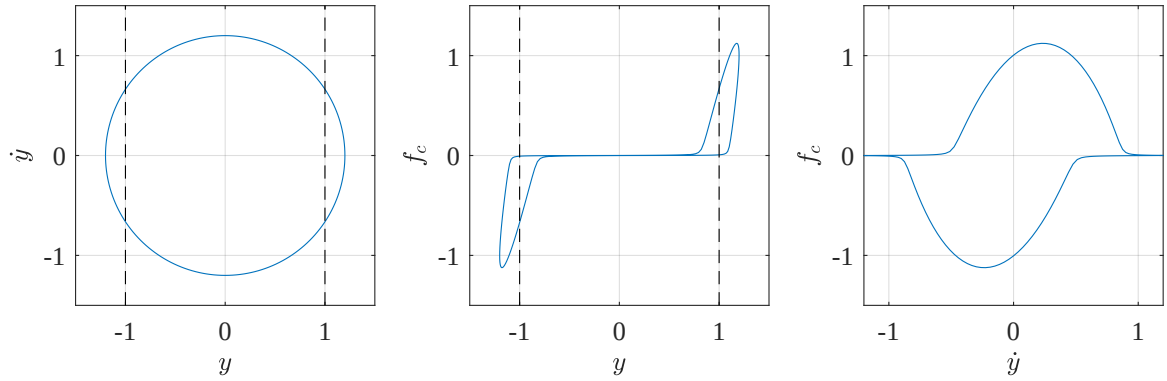

Figure 1: Illustration of the smooth impact function, with an assumed periodic displacement $y(t) = 1.2\cos(2\pi t)$ and parameters: $k_c = 5$, $c_c = 1$, $g_k = 1$, $\eta = 10^{-4}$. Dashed lines represent the contact locations.

with $\alpha_0 = 1 - \sum_{k=1}^{n_e} \alpha_k$, and where $\hat{H}(\tau)$ and $\hat{\delta}$ are, respectively, the Heaviside step function and the Dirac distribution. These effectively hard-wire causality into the model, as they ensure that any event prior to the onset of motion at $t = 0$ has no contribution to the dynamics. The second term in Eq. (5) leads to an instantaneous restoring force which is linear in $y(x,t)$ but dependent on the square of flow velocity, thus akin to lift. The integer n_e, corresponding to the number of decaying exponentials, is the order of the approximation. As for the remaining parameters appearing in Eqs. (4) and (5), D is the tube diameter, C_D is the drag coefficient, $V(x)$ and $\rho_f(x)$ are the cross-flow velocity and density distributions of the flow, respectively, V_M is the maximum velocity, and (α_k, δ_k) are empirical constants. More precisely, convolution of displacements with the first term of Eq. (5) physically corresponds to the re-organisation of the flow field through convection and diffusion of vorticity layers following every change in tube velocity. It is worth noting that memory effects having the general form of Eq. (4) with an exponential kernel appear in a wide range of applications besides the QU model discussed herein, including visco-elastic polymers [40], aero-elasticity [34] and hybrid testing [41] in the field of mechanical engineering, neural networks [42], traffic flow models [43] and numerous examples in the life sciences [44].

2.2. Model reduction

Several strategies exist for the spatial discretization of Eq. (1). In this paper, we use an expansion as a series of linear eigenmodes. The reason behind this choice is the fact that, for the empirical coefficients of the QU model, we follow the procedure from [45] and identify fluid forces acting on the tube's first bending mode from frequency-domain experimental measurements.
First, Eq. (4) is expanded to yield:

$$f_f(x,t) = \frac{1}{2}\rho_f V D C_D \dot{y} - \frac{1}{2}\rho_f V^2 \frac{\partial C_L}{\partial y}\alpha_0 y - \frac{1}{2}\frac{V^3}{D}\frac{\partial C_L}{\partial y}\sum_{k=1}^{n_e}\alpha_k\delta_k \int_0^t e^{-\delta_k \frac{V_M}{D}\tau} y(x,t-\tau)d\tau \tag{6}$$

We then re-write the density and velocity distributions as:

$$\rho_f(x) = \bar{\rho} r(x) \qquad \bar{\rho} = \frac{1}{L}\int_0^L \rho_f(x)\mathrm{d}x \tag{7}$$

$$V(x) = V_M \nu(x) \qquad V_M = \max_x |V(x)| \tag{8}$$

before introducing the modal decomposition:

$$y(x,t) = \mathbf{\Phi}(x)\mathbf{q}(t) \tag{9}$$

where $\mathbf{\Phi}(x) = [\boldsymbol{\phi}_1 ... \boldsymbol{\phi}_m] \in \mathbb{R}^{n\times m}$ is the matrix of normalized eigenvectors for the underlying undamped, unforced linear problem. Thus, the modal projection of fluid-elastic forces is given by:

$$\mathbf{f}_f(t) = V_M \mathbf{C}_f \dot{\mathbf{q}} + V_M^2 \mathbf{K}_f \mathbf{q} + V_M^3 \sum_{k=1}^{n_e} \mathbf{L}_k (\bar{h}_k * \mathbf{q}) \tag{10}$$

with the coefficient matrices given by:

$$\mathbf{C}_f = \frac{1}{2}\bar{\rho} D C_D \mathbf{L}_C \quad = \quad \frac{1}{2}\bar{\rho} D C_D \left[\frac{1}{L} \int_0^L r(x) \nu(x) \mathbf{\Phi}^T(x) \mathbf{\Phi}(x) \mathrm{d}x \right] \tag{11}$$

$$\mathbf{K}_f = -\frac{1}{2}\bar{\rho} \frac{\partial C_L}{\partial y} \alpha_0 \mathbf{L}_K \quad = \quad -\frac{1}{2}\bar{\rho} \frac{\partial C_L}{\partial y} \alpha_0 \left[\frac{1}{L} \int_0^L r(x) \nu^2(x) \mathbf{\Phi}^T(x) \mathbf{\Phi}(x) \mathrm{d}x \right] \tag{12}$$

$$\mathbf{L}_k = -\frac{1}{2}\bar{\rho} \frac{1}{D} \frac{\partial C_L}{\partial y} \alpha_k \delta_k \hat{\mathbf{L}}_k = -\frac{1}{2}\bar{\rho} \frac{1}{D} \frac{\partial C_L}{\partial y} \alpha_k \delta_k \left[\frac{1}{L} \int_0^L r(x) \nu^3(x) \mathbf{\Phi}^T(x) \mathbf{\Phi}(x) \mathrm{d}x \right] \tag{13}$$

Eqs. (11) through (13) take into account arbitrary distributions of fluid density and velocity along the tube. Regardless of the former, it is clear that matrices $\mathbf{L}_C$, $\mathbf{L}_K$ and $\hat{\mathbf{L}}_i, i = 1, n_e$ will all be equal in uniform flow, i.e. $\nu(\mathbf{x}) = 1$. This very idealized scenario is explored in Sect. 4.1, while a more realistic distribution is considered in Sect. 4.2. For the sake of simplicity, we will write $V \equiv V_M$ for the remainder of this paper. The full equations of motion in the truncated modal basis read:

$$\mathbf{M}\ddot{\mathbf{q}} + \mathbf{C}\dot{\mathbf{q}} + \mathbf{K}\mathbf{q} + \left[V\mathbf{C}_f \dot{\mathbf{q}} + V^2 \mathbf{K}_f \mathbf{q} + V^3 \sum_{k=1}^{n_e} \mathbf{L}_k \left(\bar{h}_k * \mathbf{q} \right) + \mathbf{f}_c(\mathbf{q}, \dot{\mathbf{q}}) \right] = \mathbf{0} \tag{14}$$

where the brackets group all the terms additional to the dynamics of the damped linear structure. It is clear that the quantities $\|\mathbf{q}(t)\|$, ω (the as-yet unknown limit cycle frequency) and V are of dissimilar orders of magnitude; indeed, the first of these is about the size of the smallest gap (typically a fraction of a millimetre), the second can be expected to be of the order of the tube's first natural frequency ($\sim 10^2$ rad/s), and the latter -which will take the role of the main continuation parameter- is between 1 and 7 m/s. Thus, to facilitate continuation, the following non-dimensional displacements and time are introduced: $\mathbf{q}(t) = \bar{\mathbf{q}}(t) \min_k (g_k)$, $t = \bar{t}/\omega_1$, where the latter makes use of the first-mode natural frequency. This leads to all quantities of interest being of the same order of magnitude. Moving forward, it shall be noted that the original notations $\mathbf{q}(t)$ and t will, nevertheless, be kept in order to simplify the presentation.

2.3. Formulation with internal variables

Using decaying exponentials $\bar{h}_k(t)$ as kernel functions has the effect of continuously weighting the contributions of past motions to the current state of the system, in such a way that recent events have a larger impact than those in distant pasts, which vanish in time. Besides being physically meaningful, this kernel has the supplementary advantage of leading to a convenient alternate form by introducing the n_e internal variables defined by: $\mathbf{v}_k(t) = (\hat{g}_k * \mathbf{q})(t)$. By applying Leibniz's integral rule to each internal variable and realizing $\mathbf{v}_k(0) = \mathbf{0}$ by definition for all k, it results that Eq. (14) is equivalent to the mixed-order dynamical system:

$$\begin{cases} \mathbf{M}_{s+f}\ddot{\mathbf{q}} + \mathbf{C}_s\dot{\mathbf{q}} + \mathbf{K}_s\mathbf{q} + \left[\mathbf{C}_f\dot{\mathbf{q}} + \mathbf{K}_f\mathbf{q} + \sum_{k=1}^{n_e} \mathbf{L}_k\mathbf{v}_k + \mathbf{f}_c(\mathbf{q}, \dot{\mathbf{q}}) \right] = \mathbf{0} \\ \dot{\mathbf{v}}_1 + a1\mathbf{v}_1 = \mathbf{q} \\ \vdots \\ \dot{\mathbf{v}}_{n_e} + a_{n_e}\mathbf{v}_{n_e} = \mathbf{q} \end{cases} \tag{15}$$

with $a_k = \delta_k V/D$. Eq. (15) is simpler in the sense that the explicit computation of convolution integrals is avoided, but this comes at the price of increasing the system size. As we will show in Sect. (3), this inconvenience can be circumvented in the frequency domain.

3. Numerical method

3.1. Static equilibria & Hopf bifurcation

By letting $\ddot{\mathbf{q}} = \dot{\mathbf{q}} = \mathbf{0}$ in Eq. (15), it follows that $\mathbf{q}_0 = \mathbf{0}$ is the only equilibrium of the system. Its stability is given by the eigenvalues of the tangent matrix $\mathbf{A}$:

$$\mathbf{A} = \begin{bmatrix} \mathbf{0}_n & \mathbf{I}_n & \mathbf{0}_n & \cdots & \mathbf{0}_n \\ -\mathbf{M}^{-1}(\mathbf{K}_s + \mathbf{K}_f) & -\mathbf{M}^{-1}(\mathbf{C}_s + \mathbf{C}_f) & -\mathbf{M}^{-1}\mathbf{L}_1 & \cdots & -\mathbf{M}^{-1}\mathbf{L}_{n_e} \\ \mathbf{I}_n & \mathbf{0}_n & -a_1\mathbf{I}_n & \cdots & \mathbf{0}_n \\ \vdots & \vdots & \vdots & \ddots & \vdots \\ \mathbf{I}_n & \mathbf{0}_n & \mathbf{0}_n & \cdots & -a_{n_e}\mathbf{I}_n \end{bmatrix} \tag{16}$$

In particular, these eigenvalues depend on V through the fluid-related terms: $\mathbf{K}_f$, $\mathbf{C}_f$, a_k, $\mathbf{L}_k$, and there exists a value $V = V_c$ such that $\mathbf{q}_0$ loses stability through a Hopf bifurcation. At this point, a branch of limit cycles with growing amplitude emerges, whose computation and bifurcation analysis will be our main focus for the remainder of this paper.

3.2. HBM treatment of fluid-elastic forces

An approximate solution is sought in two steps. Firstly, the steady state solution $\mathbf{q}(t)$ is assumed to be expressible by a series expansion over a certain basis $\mathbb{B}_1(t)$ of orthonormal functions with period T. Secondly, this expansion is introduced in the equations of motion, which are then projected onto an orthonormal basis $\mathbb{B}_2(t)$ through an adequate scalar product. In the classical HBM, a basis of trigonometric functions is used for both expansion and projection, which results is an algebraic problem for the Fourier coefficients of $\mathbf{q}(t)$. This requires choosing $\mathbb{B}_1(t) = \mathbb{B}_2(t) = \mathbb{F}_H(\omega t) \in C^\infty\left(\mathbb{R}^L, [0, T = 2\pi/\omega]\right)$, with $L = 2H + 1$, such that:

$$\mathbb{F}_H(\omega t) = \begin{bmatrix} 1 & \cos(\omega t) & \sin(\omega t) & \dots & \cos(H\omega t) & \sin(H\omega t) \end{bmatrix} \tag{17}$$

where ω is the fundamental circular frequency of oscillation and the expansion is truncated at the H-th harmonic. Hence, $\mathbf{q}(t) \in \mathbb{R}^n$ can be uniquely expressed in terms of its Fourier coefficients, $\mathbf{Q} \in \mathbb{R}^{nL}$:

$$\mathbf{q}(t) = (\mathbb{F}_H(\omega t) \otimes \mathbf{I}_n)\,\mathbf{Q} \tag{18}$$

The symbol $\otimes$ stands for the Kronecker tensor product. The Fourier coefficients are grouped in vector $\mathbf{Q}$. Time-derivatives of $\mathbf{q}(t)$ are proportional to $\mathbf{Q}$ as well, since only the basis functions are time-dependent. More precisely:

$$\dot{\mathbf{q}}(t) = \omega(\mathbb{F}_H(\omega t)\nabla \otimes \mathbf{I}_n)\mathbf{Q} \tag{19}$$

where the operator $\nabla \in \mathbb{R}^{L\times L}$ applies a permutation to the basis functions, as follows:

$$\begin{aligned} \nabla &= \mathrm{diag}\,(0, \nabla_1, ..., \nabla_H) \\ \forall j = 1, ..., H \quad &: \quad \nabla_j = j\begin{bmatrix} 0 & 1 \\ -1 & 0 \end{bmatrix} \end{aligned} \tag{20}$$

Considering Eq. (15), it should be noted that a periodic $\mathbf{q}(t)$ implies the same periodicity for the $\mathbf{v}_k(t)$ and nonlinear forces $\mathbf{f}_c$. Thus, the Fourier-Galerkin method is applied to yield:

$$\begin{cases} \mathbf{Z}(\omega)\mathbf{Q} + \displaystyle\sum_{k=1}^{n_e} \mathbf{L}_k\mathbf{V}_k + \mathbf{F}_{NL}(\mathbf{Q}, \omega) = \mathbf{0} \\ \left[a_k\mathbf{I}_L + \omega(\nabla \otimes \mathbf{I}_n)\right]\mathbf{V}_1 \;\; = \mathbf{Q} \\ \vdots \\ \left[a_{n_e}\mathbf{I}_L + \omega(\nabla \otimes \mathbf{I}_n)\right]\mathbf{V}_{n_e} = \mathbf{Q} \end{cases} \tag{21}$$

The Fourier coefficients of nonlinear forces, $\mathbf{F}_{NL}(\mathbf{Q})$, are computed through the Alternating Frequency-Time (AFT) method [46]. Here, the fluid-elastic dynamic stiffness matrix $\mathbf{Z}(\omega, V) \in \mathbb{R}^{nL\times nL}$ is given by:

$$\mathbf{Z}(\omega, V) = \omega^2\nabla^2 \otimes \mathbf{M}_{s+f} + \omega\nabla \otimes \left(\mathbf{C}_s + V\mathbf{C}_f\right) + \mathbf{I}_L \otimes \left(\mathbf{K}_s + V^2\mathbf{K}_f\right) \tag{22}$$

Moving forward, for the sake of conciseness, the subscripts $s{+}f$ will be dropped, and the matrices $\mathbf{M}, \mathbf{C}, \mathbf{K}$ include both structure and fluid contributions. Eq.(21) could be solved directly by Newton-Raphson iterations, treating the $\mathbf{V}_k$ as additional unknowns. However, this unnecessarily increases the system size, as the Fourier coefficients of the internal variables are proportional to $\mathbf{Q}$. Indeed, for all $a_k \neq 0$, the matrices $[a_k\mathbf{I}_L + \omega(\nabla \otimes \mathbf{I}_n)]$ admit the inverses:

$$\mathbf{S}_k(\omega, V) = (\mathbf{B}_k(\omega, V) \otimes \mathbf{I}_n)\,[a_k\mathbf{I}_L - \omega\nabla \otimes \mathbf{I}_n] \tag{23}$$

where:

$$\mathbf{B}_k(\omega, V) = \mathrm{diag}\left(1/a_k^2, \frac{1}{a_k^2+\omega^2}\begin{bmatrix} 1 & 0 \\ 0 & 1 \end{bmatrix}, ..., \frac{1}{a_k^2+(H\omega)^2}\begin{bmatrix} 1 & 0 \\ 0 & 1 \end{bmatrix}\right)$$

Eq. (23), actually, describes nothing more than the Laplace transform of a decaying exponential function evaluated at the discrete values $\{0, \omega, ..., H\omega\}$, with the real parts along the diagonal and the imaginary parts as the elements of a skew-symmetric matrix. Respectively, these contribute additional stiffness and (negative) damping terms to the equations of dynamic equilibrium, which read:

$$\mathbf{R}(\mathbf{Q}, \omega, V) = \left[\mathbf{Z}(\omega, V) + \sum_{k=1}^{n_e} \mathbf{S}_k(\omega, V) \otimes \mathbf{L}_k\right]\mathbf{Q} + \mathbf{F}_{NL}(\mathbf{Q}, \omega) = \mathbf{0} \tag{24}$$

Given a fixed velocity V, finding an approximate periodic solution - correct up to the H-th harmonic- is equivalent to finding roots of the residual function, $\mathbf{R}(\mathbf{X}, \omega)$, which is a frequency-domain expression of dynamic equilibrium. Furthermore, the fact that the system is autonomous implies that the circular frequency is unknown *a priori* and must be found simultaneously with the Fourier coefficients. The problem $\mathbf{R}(\mathbf{X}, \omega) = \mathbf{0}$ is under-constrained and must be completed by an additional equation. This is done here by introducing a *phase condition* which fixes a nil initial phase for the first degree-of-freedom, i.e. : $\dot{x}_1(0) = 0$, which entails no loss of generality. In the frequency domain, this reads:

$$g(\mathbf{Q}) = \mathbf{e}_0\mathbf{Q} = 0, \qquad \text{where:} \qquad \mathbf{e}_0 = [0\ \ 0\ \ 1\ \ 0\ \ 2\ \ \ldots\ \ 0\ \ (H-1)\ \ 0\ \ H] \otimes [1\ \ 0\ \ \ldots\ \ 0] \tag{25}$$

The problem $\mathbf{Y}_\mathrm{A}(\mathbf{Q}, \omega) = \left[\mathbf{R}^T(\mathbf{Q}, \omega)\ \ g(\mathbf{Q})\right]^T = \mathbf{0}$ is well-posed and may be solved iteratively.

3.3. Stability and bifurcations

The evaluation of local stability around a cycle $\mathbf{q}_0(t)$ is sought by applying a perturbation $\boldsymbol{\eta}(t)$ to Eq. (15), i.e. by letting $\mathbf{q}(t) = \mathbf{q}_0(t) + \boldsymbol{\eta}(t)$ in the equations of motion. The perturbation evolves in time according to:

$$\mathbf{M}\ddot{\boldsymbol{\eta}}(t) + \left[\mathbf{C} + \left(\frac{\partial \mathbf{f}_\mathrm{NL}}{\partial \dot{\mathbf{q}}}\right)_{\dot{\mathbf{q}}_0(t)}\right]\dot{\boldsymbol{\eta}}(t) + \left[\mathbf{K} + \left(\frac{\partial \mathbf{f}_\mathrm{NL}}{\partial \mathbf{q}}\right)_{\mathbf{q}_0(t)}\right]\boldsymbol{\eta}(t) + \sum_{k=1}^{n_e}\mathbf{L}_k\int_0^t e^{-a_k\tau}\boldsymbol{\eta}(t-\tau)d\tau = \mathbf{0} \tag{26}$$

Let us define the state vector $\mathbf{z}(t) = [\boldsymbol{\eta}^T(t), \dot{\boldsymbol{\eta}}^T(t), \boldsymbol{\zeta}_1^T(t), ..., \boldsymbol{\zeta}_{n_e}^T(t)]^T$, where each of the $\boldsymbol{\zeta}_k^T(t)$ vectors ($k = 1, ..., n_e$) stands for the k-th convolution term for the perturbation. The system's state is described equivalently by the first-order ODE:

$$\dot{\mathbf{z}}(t) = \mathbf{A}(t)\mathbf{z} \tag{27}$$

with the periodic coefficient matrix:

$$\mathbf{A}(t) = \begin{bmatrix} \mathbf{0}_n & \mathbf{I}_n & \mathbf{0}_n & \cdots & \mathbf{0}_n \\ -\mathbf{M}^{-1}\left[\mathbf{K} + \left(\frac{\partial \mathbf{f}_\mathrm{NL}}{\partial \mathbf{q}}\right)_{\mathbf{q}_0(t)}\right] & -\mathbf{M}^{-1}\left[\mathbf{C} + \left(\frac{\partial \mathbf{f}_\mathrm{NL}}{\partial \dot{\mathbf{q}}}\right)_{\dot{\mathbf{q}}_0(t)}\right] & -\mathbf{M}^{-1}\mathbf{L}_1 & \cdots & -\mathbf{M}^{-1}\mathbf{L}_{n_e} \\ \mathbf{I}_n & \mathbf{0}_n & -a_1\mathbf{I}_n & \cdots & \mathbf{0}_n \\ \vdots & \vdots & \vdots & \ddots & \vdots \\ \mathbf{I}_n & \mathbf{0}_n & \mathbf{0}_n & \cdots & -a_{n_e}\mathbf{I}_n \end{bmatrix} \tag{28}$$

From Floquet theory, the $n(2 + n_e)$ solutions of Eq. (27) have the form $\mathbf{z}_i(t) = e^{\lambda_i t}\mathbf{p}_i(t)$, where $\mathbf{p}(t) \in \mathbb{R}^{n(2+n_e)}$ has the same periodicity as the underlying limit cycle. Each of the vectors making up $\mathbf{z}(t)$ can thus be written as an independent Fourier series, for instance:

$$\mathbf{p}_i(t) = \left[\mathbf{I}_{2+n_e} \otimes (\mathbf{\Gamma}_H \otimes \mathbf{I}_n)\right] \boldsymbol{\phi}_i \tag{29}$$

Hence, expanding the left-hand side derivative and applying harmonic balance independently to each block-wise row leads to the linear eigenvalue problem:

$$\mathbb{H}\boldsymbol{\phi}_i = \lambda_i \boldsymbol{\phi}_i \tag{30}$$

$$\mathbb{H} = \begin{bmatrix} -\omega\nabla \otimes \mathbf{I}_n & \mathbf{I}_{nL} & \mathbf{0}_{nL} & \cdots & \mathbf{0}_{nL} \\ \mathbf{H}_{\mathrm{K}} & \mathbf{H}_{\mathrm{C}} & -\mathbf{I}_L \otimes (\mathbf{M}^{-1}\mathbf{L}_1) & \cdots & -\mathbf{I}_L \otimes (\mathbf{M}^{-1}\mathbf{L}_{n_e}) \\ \mathbf{I}_{nL} & \mathbf{0}_{nL} & -\omega\nabla \otimes \mathbf{I}_n - a_1\mathbf{I}_{nL} & \cdots & \mathbf{0}_{nL} \\ \vdots & \vdots & \vdots & \ddots & \vdots \\ \mathbf{I}_{nL} & \mathbf{0}_{nL} & \mathbf{0}_{nL} & \cdots & -\omega\nabla \otimes \mathbf{I}_n - a_{n_e}\mathbf{I}_{nL} \end{bmatrix} \tag{31}$$

$$\mathbf{H}_{\mathrm{K}} = -(\mathbf{I}_L \otimes \mathbf{M}^{-1})\left[\mathbf{I}_L \otimes \mathbf{K} + \frac{\partial \mathbf{F}_{\mathrm{NL}}}{\partial \mathbf{Q}}\right] \qquad \mathbf{H}_{\mathrm{C}} = -\omega\nabla \otimes \mathbf{I}_n - (\mathbf{I}_L \otimes \mathbf{M}^{-1})\left[\mathbf{I}_L \otimes \mathbf{C} + \frac{\partial \mathbf{F}_{\mathrm{NL}}}{\partial \mathbf{Q}'}\right]$$

The derivatives featured in matrices $\mathbf{H}_{\mathrm{K}}$ and $\mathbf{H}_{\mathrm{C}}$ are computed by the AFT method [47], and correspond to:

$$\frac{\partial \mathbf{F}_{\mathrm{NL}}}{\partial \mathbf{Q}} = (\mathbb{F}_H(\omega t) \otimes \mathbf{I}_n)^{-1}\left(\frac{\partial \mathbf{f}_{\mathrm{NL}}}{\partial \mathbf{q}}\right)_{\mathbf{q}_0(t)} (\mathbb{F}_H(\omega t) \otimes \mathbf{I}_n) \qquad \frac{\partial \mathbf{F}_{\mathrm{NL}}}{\partial \mathbf{Q}'} = (\mathbb{F}_H(\omega t) \otimes \mathbf{I}_n)^{-1}\left(\frac{\partial \mathbf{f}_{\mathrm{NL}}}{\partial \dot{\mathbf{q}}}\right)_{\mathbf{q}_0(t)} (\mathbb{F}_H(\omega t) \otimes \mathbf{I}_n)$$

Eq. (30) admits $(2+n_e)nL$ solutions, from which only $(2+n_e)n$ eigenvalues truly correspond to the Floquet Exponents (FEs) of the system and the rest are redundant. A selection is performed by choosing the eigenvalues whose imaginary parts lie in the interval $[-\omega/2, \omega/2]$, whose number is exactly $(2 + n_e)nL$ if convergence (in terms of number of harmonics) has been achieved [48]. A stable cycle is characterized by having only FEs with strictly negative real parts.

Furthermore, special attention must be given to the fact that one of the FEs is always theoretically zero because Eq. (14) is autonomous. Due to numerical errors, this trivial exponent has a small but non-zero value in practice, whose sign might change and be spuriously interpreted as a bifurcation. To resolve this issue, the trivial zero exponent is shifted by using the standard technique [49] on the matrix $\mathbb{H}$. This requires the associated eigenvector to be known, which is the case here. Indeed, it can be shown (see Appendix A) that the sought eigenvector is equal to:

$$\boldsymbol{\phi}_0 = \begin{bmatrix} \boldsymbol{\phi}_p \\ \omega(\nabla \otimes \mathbf{I}_n)\boldsymbol{\phi}_p \\ \mathbf{S}_1(\omega)\boldsymbol{\phi}_p \\ \vdots \\ \mathbf{S}_{n_e}(\omega)\boldsymbol{\phi}_p \end{bmatrix} \tag{32}$$

where $\boldsymbol{\phi}_p = (\nabla \otimes \mathbf{I}_n)\mathbf{Q}$, with $\mathbf{Q}$ and ω corresponding to a given periodic solution $\mathbf{q}_0(t)$. As is typically done in the context of numerical continuation, changes in the number of Floquet exponents with positive real values between two consecutive steps indicate the presence of a nearby bifurcation, which is then precisely localized by solving an appropriate extended system. In this paper, the different codimension-1 bifurcations are labelled as follows:

- **LP** : *limit point*, also known as *saddle-node* or *fold* bifurcation of cycles, occurs when a Floquet exponent is equal to 0 and non-degeneracy conditions are met [50]. This exponent has an algebraic multiplicity of two but geometric multiplicity of one. In other words, the null-space of the cycle is spanned by a single eigenvector, and so there exists a generalized eigenvector $\boldsymbol{\psi}$ associated to the zero exponent which forms a Jordan chain along with $\boldsymbol{\psi}_p$. Geometrically, this bifurcation manifests as a vertical tangent with respect to the continuation parameter. Letting $\mathbf{D}_1$ be the unique matrix such that: $\mathbf{R}_\omega = \mathbf{D}_1(\nabla \otimes \mathbf{I}_n)\mathbf{Q}$, an extended system characterizing this bifurcation is thus:

$$\mathbf{Y}^{\mathrm{LP}}(\mathbf{Q}, \omega, V, \boldsymbol{\psi}) = \begin{bmatrix} \mathbf{R} \\ g \\ \mathbf{R}_{\mathbf{Q}}\boldsymbol{\psi} + \mathbf{D}_1\boldsymbol{\phi}_p \\ \boldsymbol{\psi}^t\boldsymbol{\phi}_p \end{bmatrix} = \mathbf{0} \tag{33}$$

- **BP** : *branching point*, also known as *pitchfork* or *symmetry-breaking* bifurcation. A Floquet exponent is equal to 0 but this singularity is degenerate, meaning that there exists an eigenvector $\boldsymbol{\psi}$ which spans the null-space along with $\boldsymbol{\phi}_p$. In other words, two different tangents exist locally at the bifurcation point. As this provides an additional constraint on the extended system, an artificial parameter $\gamma = 0$ can be introduced to yield a well-posed problem:

$$\mathbf{Y}^{\mathrm{BP}}(\mathbf{Q}, \omega, V, \boldsymbol{\psi}, \gamma) = \begin{bmatrix} \mathbf{R} + \gamma \boldsymbol{\phi}_p \\ g \\ \mathbf{R}_{\mathbf{Q}}^t \boldsymbol{\psi} \\ \boldsymbol{\psi}^t \mathbf{R}_\omega \\ ||\boldsymbol{\psi}||^2 - 1 \end{bmatrix} = \mathbf{0} \tag{34}$$

  Periodic solutions along the emerging branch are still periodic but qualitatively different those in the original branch. This may involve, for instance, a formerly-inactive degree of freedom becoming active, or non-zero contributions from the even harmonics in the Fourier series of the cycles.

- **NS** : *Neimark-Sacker* or *torus* bifurcation. A branch of quasi-periodic solutions emerges from the bifurcation point. In this case, the critical Floquet exponents are purely imaginary and conjugate: $\lambda = \pm i\kappa$, so the eigenvector is complex: $\boldsymbol{\psi} = \boldsymbol{\psi}_R \mp i\boldsymbol{\psi}_I$. Two normalization conditions must be appended to close the system, for instance: one to fix the total norm and one to impose the maximum value of a given component of $\boldsymbol{\psi}_R$, see [51] for a justification of this choice.

$$\mathbf{Y}^{\mathrm{NS}}(\mathbf{Q}, \boldsymbol{\psi}_R, \boldsymbol{\psi}_I, \omega, \kappa, V) = \begin{bmatrix} \mathbf{R}(\mathbf{Q}, \omega, V) \\ \mathbb{H}(\mathbf{Q}, \omega, V)\boldsymbol{\psi}_R - \kappa\boldsymbol{\psi}_I \\ \kappa\boldsymbol{\psi}_R + \mathbb{H}(\mathbf{Q}, \omega, V)\boldsymbol{\psi}_I \\ g(\mathbf{Q}) \\ ||\boldsymbol{\psi}_R||^2 + ||\boldsymbol{\psi}_I||^2 - 1 \\ \mathbf{p}_a^T \boldsymbol{\psi}_R \end{bmatrix} = \mathbf{0} \tag{35}$$

- **PD**: *period-doubling* or *flip* bifurcation of cycles. Limit case of a NS bifurcation where the new frequency $\kappa = \omega/2$. At this point, a new branch of subharmonic periodic cycles emerges. It shall be noted that this type of bifurcation is not studied in the present paper.

4. Applications

For the examples presented in this section, we use the QU coefficients from [45], collected in Table 1. Their computations showed a good fit to experimental results by using a second-order kernel, i.e. $k = 2$.

	$k = 1$	$k = 2$
α_k	1.2581	-2.2583
δ_k	0.2209	32.1219

Table 1: Empirical coefficients for the QU model with two-term memory.

The numerical methods described in the previous section were implemented into a MATLAB continuation environment that has long been developed by the authors.

4.1. Cantilever beam in cross-flow

The system is depicted in Fig. 2. A single flexible tube in a rigid square array is subjected to single-phase, spatially uniform, liquid water cross-flow. Its geometry is designed to allow motions in the lift (transverse) direction only. Symmetrical stops are located at the coordinate $x_c = 0.624L$, where L is the total tube length. On each side, the gaps have the value: $g = 1.5$ mm, but the numerical model is scaled so that they correspond to a value of $y_c = 1$, where y_c is the non-dimensional transverse displacement at the stop location, computed through modal recombination. Modal

Mode	1	2	3	4	5
Frequency (non-dimensional)	1.0	11.67	42.20	73.86	130.92
Mass (kg)	0.15682	0.27256	0.15608	0.16551	0.17557

Table 2: Modal properties for the cantilever tube.

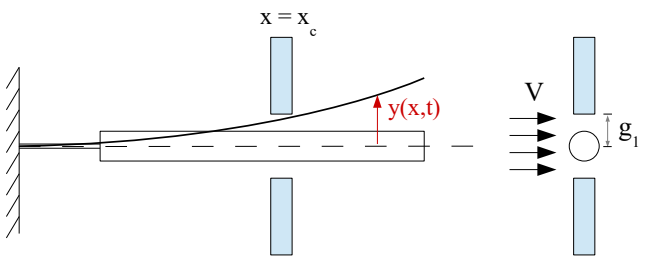

Figure 2: Cantilever tube in loose support.

properties of the linear system in stagnant fluid were found by using a finite-element representation in Cast3M [52]. The properties of the first five modes are collected in Table 2.

Eigenfrequencies have been scaled by the first-mode angular frequency, $\omega_1 = 120.4110$ rad/s. In this section, the behaviour of the one-mode approximation is explored by continuation, leading to a global picture of its dynamics that was lacking from previous studies. Furthermore, the effect of including additional modes is investigated. A fixed number of 50 harmonics with $N_s = 2^{12}$ AFT samples was used throughout, with $\eta = 0.5 \cdot 10^{-5}$ for the regularization of impacts.

4.1.1. 1-mode model

The stability analysis of equilibria, as per Sect. 3.1, shows that $V_c = 2.079$ m/s. At this point, a branch of neutrally-stable periodic solutions emerges, with fixed frequency and steadily-growing amplitude until impacts start happening, as shown in Fig. 3 a). An alternate representation is presented in Fig. 3 b), where the maximal (non-dimensional) impact force over one cycle is plotted instead of the norm of Fourier coefficients, $\|\mathbf{Q}\|$.

Three branches of periodic solutions bifurcate from the starting point of impact. The lower branch (in terms of the associated contact forces) consists of symmetric solutions and is unstable for low flow velocities, up until the BP at $V_{\mathrm{BP}} = 3.239$ m/s. Meanwhile, the upper branches are stable and consist of asymmetric solutions. Moreover, these branches are mirror images of one another, i.e.: the only difference between them is a negative sign in their Fourier coefficients; this comes from the fact that the symmetry of the system can be broken in either the positive or the negative direction, similarly to a buckled beam or plate. Hence, these branches overlap in the projection shown in this figure and only one curve is visible. Interestingly, stable cycles of both kinds coexist between V_{BP} and $V_{\mathrm{LP}} = 3.822$ m/s. In this region, the symmetric and asymmetric solutions are linked by unstable transition branches which ensure a smooth evolution from one behaviour to the other, as could be expected from an equation with continuous dependence on the parameter V. Solutions in the symmetric branch undergo two impacts per period, whereas there is only one in the symmetric branches. Thus, transition cycles are both two-impacts-per-period and asymmetric. Examples of solutions are presented in Fig. 4, showing all five coexisting regimes for $V = 3.4$ m/s. For $V > V_{\mathrm{LP}}$, only symmetric cycles exist; this is due to the energy input from the flow being so high that the tube's motion inevitably attains both supports. It shall be noted that knowledge of the bi-stability region is important for practical applications, since the state of the system can "jump" from one branch to the other due to disturbances coming from, e.g., turbulence, such that a predictive computation of forces and wear over time becomes difficult. Thus, the range $V_{BP} \leq V \leq V_{LP}$ defines an unsafe operating region that should be avoided.

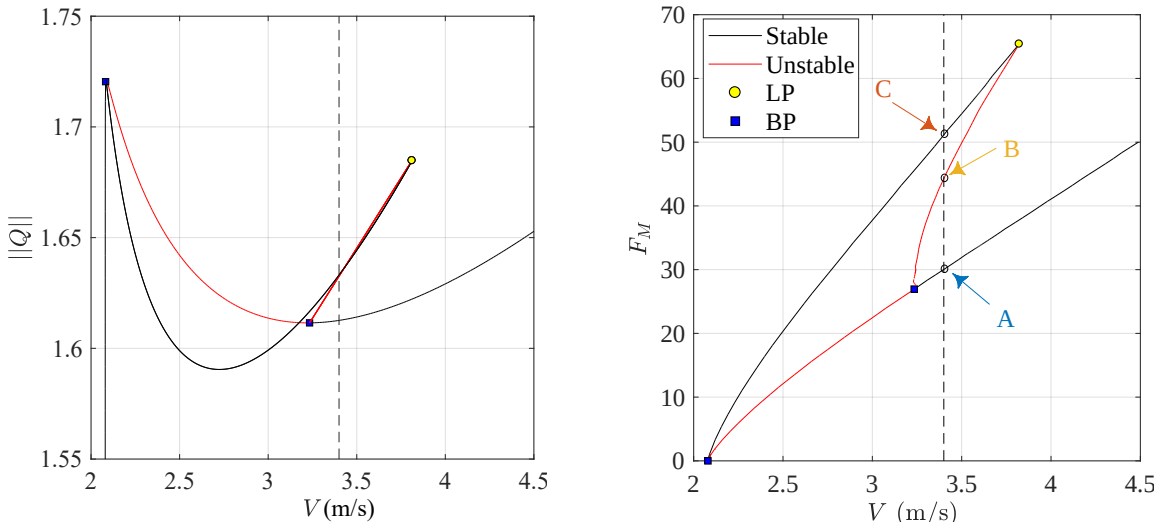

Figure 3: Continuation of periodic solutions for one-mode model for V as continuation parameter, with ordinates: a) norm of Fourier coefficient vector, b) maximum contact force (in absolute value) over one cycle. (——) stable branch, (——) unstable branch. As per Sect. 3 bifurcations are labeled: ○ LP, ■ BP.

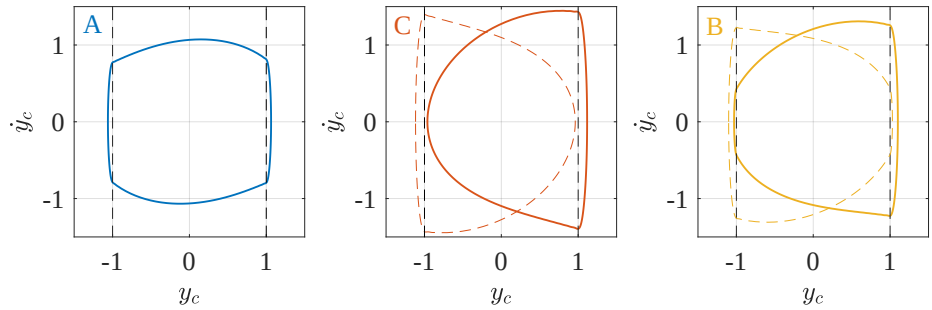

Figure 4: Phase-space representation of converged cycles for $V = 3.4$ m/s, at the support location x_c. Letters are associated with points on Fig. 3 b). Dashed cycles in the two right-most diagrams correspond to the solutions on the twin asymmetric branches.

A note on stability computation. From the fact that K_c is large with respect to the system's stiffness, the contact duration is small compared to the oscillation period. Impacts are thus localized events in time, which demand a considerable number of samples N_s in the AFT procedure to be correctly resolved. However, while this certainly affects the accuracy of the computed impact forces, its effect is much more dramatic on the their derivatives, which tend to step functions as $\eta \to 0$. Consequently, the appearance of the Gibbs phenomenon is to be expected. This is very relevant for stability evaluation and bifurcation analysis, since these derivatives directly intervene in the computation of the Hill matrix as per Eq. (31). Fig. 5 shows how the real parts of the Floquet exponents, along the continuation of the symmetric branch, vary with N_s. The moderate choice $N_s = 2^8$ leads to unusable results, as two exponents spuriously cross the stability boundary in an oscillatory fashion. Increasing to $N_s = 2^{10}$ attenuates this problem, but the trivial Floquet exponent is still not exactly zero, as discussed in Sect. 3.3. Fig. 5 displays a correct and unambiguous stability evaluation, performed by filtering the trivial zero through the proposed technique. It should be noted, nonetheless, that asymmetric solutions are seemingly more sensitive to the Gibbs phenomenon, as evidenced by Fig. 6. On these branches, spurious oscillations in the Floquet exponents persist for $N_s = 2^{12}$, but this sampling rate made them sufficiently small to allow for a proper stability evaluation.

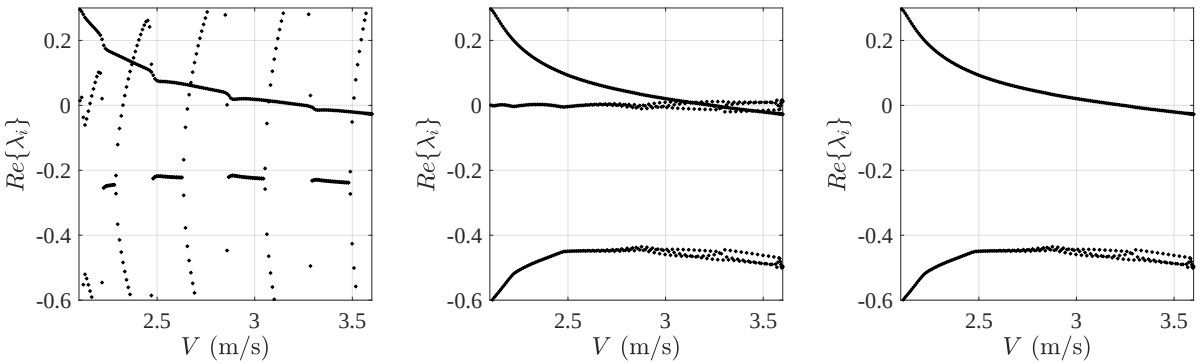

a) $N_s = 2^8$. b) $N_s = 2^{10}$. c) $N_s = 2^{10}$, filtered.

Figure 5: Real part of Floquet exponents (symmetric cycles) for different numbers of AFT samples. In c), the trivial zero is shifted to −1.

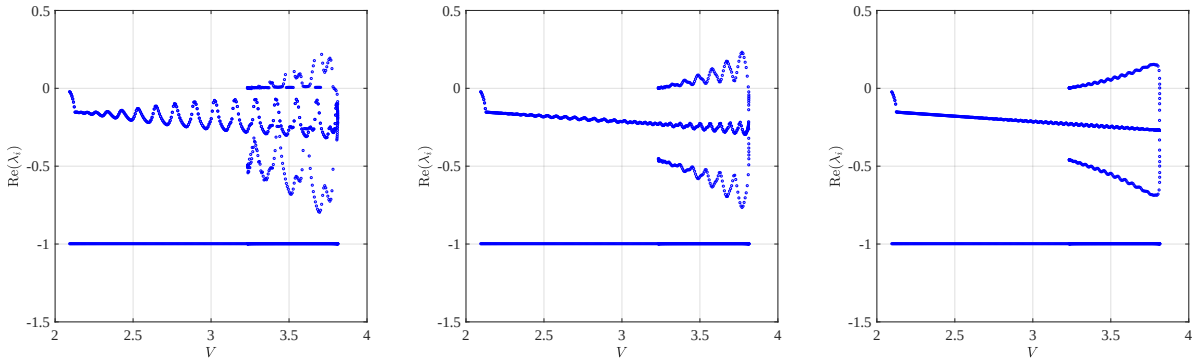

a) $N_s = 2^{10}$. b) $N_s = 2^{11}$. c) $N_s = 2^{12}$.

Figure 6: Real part of Floquet exponents (asymmetric cycles) for different numbers of AFT samples, with trivial exponent shifted to -1.

Choosing a regularization coefficient. The impact function given in Eq. (3) depends continuously on all its parameters, including η. This implies that numerical continuation can be used to assess the evolution of a given cycle upon its variation, for a fixed velocity. The idea is to choose the largest possible value for η -thus yielding a smoother function- without altering the value of a certain measure beyond some threshold, e.g. 5 per cent relative error. Here we have chosen as a measure the maximal value of impact force over one cycle, denoted F_M, as this quantity is physically meaningful. Fig. 7 shows an example for the one-mode cantilever beam at $V = 3.6$ m/s. As expected, F_M converges as η is reduced. On the other hand, it is clear that choosing an overly large value of η leads to completely erroneous results. This is most notable in the case of the asymmetric branch, whose two coexisting cycles meet at a LP at $\eta_{LP} = 4 \cdot 10^{-4}$, meaning that the branch disappears altogether for $\eta > \eta_{LP}$. This graph provides justification of the choice $\eta = 0.5 \cdot 10^{-5}$ used in this section. Clearly, there is no reason to assume that a value of η which works well for a single-mode model will remain valid for a multi-mode model, and a new convergence study should be performed if a different systems is considered.

4.1.2. 2-mode model

It is immediately evident from Fig. 8 that this approximation presents much richer dynamics, compared to the previous one. As before, representations in the $\|Q\| - V$ and $F_M - V$ planes are shown. Right after the onset of fluid-elastic instability, a similar behaviour is observed: two stable asymmetric and one unstable symmetric branch emerge. At a higher velocity, the branches meet at a BP. In between these points, however, both curves undergo a series of folds. Fig. 8 b) shows a clearer view of the pattern. Furthermore, a new BP appears at $V_{BP2} = 4.593$, but its emerging branch is not shown in this figure.

Another interesting result obtained from continuation is the fact that most cycles on both branches are unstable.

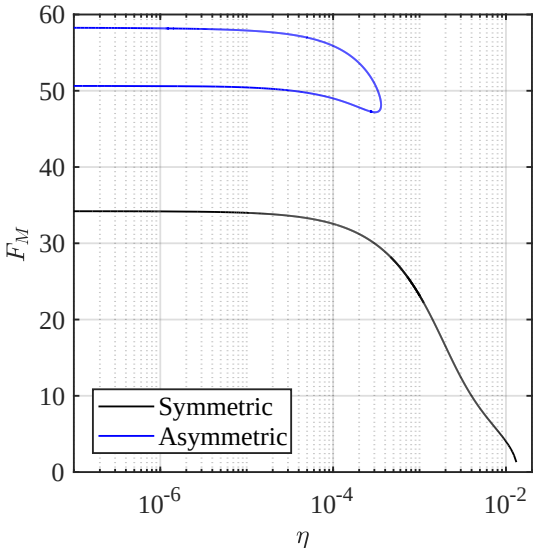

Figure 7: Continuation of coexisting cycles with respect to η for a one-mode approximation of the cantilever beam, given $V = 3.6$ m/s.

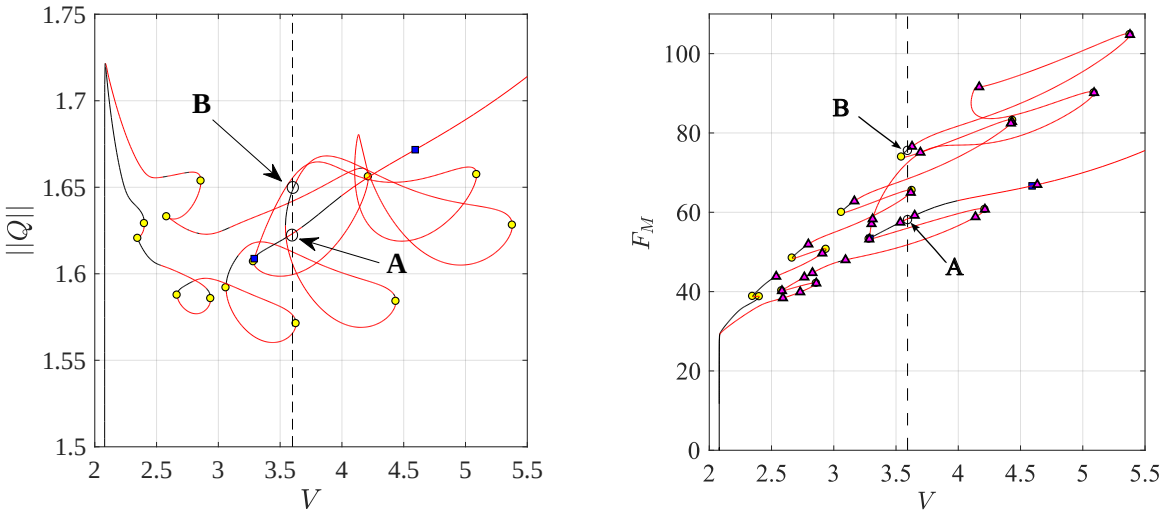

a) $||Q|| - V$ plane

b) $F_M - V$ plane

Figure 8: Continuation of periodic solutions for two-mode model: a) $\|\mathbf{Q}\| - V$ plane, b) $F_M - V$ plane. (——) stable branch, (——) unstable branch, ● LP, ▲ NS, ■ BP. It should be noted that both panels are graphical representations of the same continuation results: in particular, the NS bifurcations shown in b) are also present a), but have been omitted from the latter for enhanced readability.

Periodic solutions are thus rare, with the oscillations of modal coordinates not synchronized in most cases. The responses are then expected to be mostly quasi-periodic, a hypothesis supported by the high number of NS bifurcations found along continuation. These are shown on the $F_M - V$ plane in Fig. 8 b). Time integration through MATLAB's ode45 function was used to confirm the existence of quasi-periodic solutions on the unstable portions of the response curve, with an example shown in Fig. 9. Here, two of the HBM-predicted solutions on the symmetric and asymmetric branches, respectively labelled **A** and **B** in Fig. 8 a), are compared to ode45's solution for $V = 3.6$ m/s and represented in the configuration space of modal displacements, (q_1, q_2). As seen from inspection of Fig. 8 b), **A** lies in an unstable portion of the symmetric branch, delimited by two NS bifurcations, hinting at a quasi-periodic response. Indeed, using the unstable HBM cycle as initial condition for integration, a symmetric quasi-periodic regime is readily found

by ode45 after a short transient dies out. As clearly seen in this figure, the unstable periodic solution seems to be a support for the stable, quasi-periodic motion, i.e. averaging the latter over time would approximately yield the former. On the other hand, HBM-computed stable cycle **B** is indistinguishable from its time-integration counterpart.

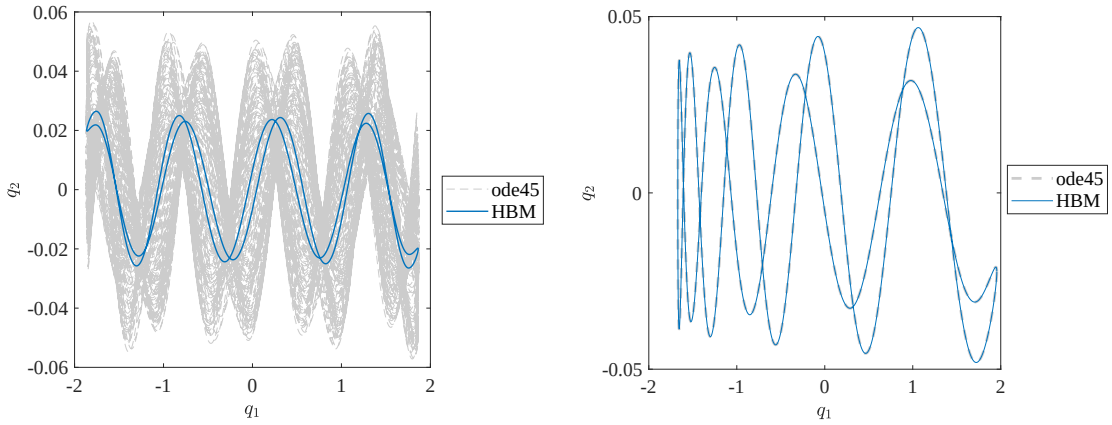

A: Symmetric cycle. **B**: Asymmetric cycle.

Figure 9: Comparison of cycles obtained by HBM and time-integration (MATLAB's ode45), for $V = 3.6$ m/s. The labels **A** and **B** refer to the cycles marked with the same letters in Fig. 8 b). The cycle **A**, close to NS bifurcations and evaluated unstable by the HBM, leads to a quasi-periodic response, whereas stable cycle **B** yields a periodic solution which is identical to the HBM prediction.

To understand the pattern of folds appearing on the aforementioned continuation curves, the frequency content of each mode needs to be analysed. This is automatic when using the HBM since modal displacements are given in time domain, from Eq. (18), by:

$$\mathbf{q}(t) = \begin{bmatrix} q_1(t) \\ \vdots \\ q_n(t) \end{bmatrix} = \begin{bmatrix} Q_0^1 + Q_{c1}^1 \cos(\omega t) + Q_{s1}^1 \sin(\omega t) + ... + Q_{cH}^1 \cos(H\omega t) + Q_{sH}^1 \sin(H\omega t) \\ \vdots \\ Q_0^n + Q_{c1}^n \cos(\omega t) + Q_{s1}^n \sin(\omega t) + ... + Q_{cH}^n \cos(H\omega t) + Q_{sH}^n \sin(H\omega t) \end{bmatrix} \tag{36}$$

where ω is the angular frequency of a given limit cycle and the coefficients Q_x^i are the components of $\mathbf{Q}$, i.e. the Fourier coefficients of each $q_i(t)$. For mode number $i = 1, ..., n$, we may quantify the contribution of a given harmonic $j = 1, ..., H$ to the total response by computing: $\|Q_j^i\| = \sqrt{(Q_{cj}^i)^2 + (Q_{sj}^i)^2}$. Along the symmetric solution branch, only odd harmonics $j = 1, 3, 5...$ are non-zero. We focus on this branch for illustration purposes and plot the harmonic amplitudes $\|Q_j^1\|$, $\|Q_j^2\|$ up until the fifteenth harmonic as a function of V in Fig. 10. The different curves in this figure are are labelled $j\omega$ to represent the j-th harmonic. Thanks to these plots, the fold pattern of Fig. 8 can be explained as a redistribution of mechanical energy from the first to the second mode due to impacts. Starting at the Hopf bifurcation defined by: $V_c = 2.079$ m/s, $\|\mathbf{Q}\| = \mathbf{0}$, only the fundamental component (1ω) of the first mode is active. As soon as the the amplitude becomes high enough for contact to take place, higher harmonics of the first mode -such as (3ω) and (5ω)- contribute to the response. Meanwhile the second mode is practically quiescent, but around $V = 3$ m/s we observe a loop in the first-mode curve which coincides with a surge in the (11ω) harmonic amplitude of the second mode. Over this flow velocity range, the amplitudes $\|Q_j^1\|$ are limited. We can thus characterize this situation as an internal resonance, where energy is transferred from the first mode to the second. This is a consequence of the natural frequencies of both modes being varying due to nonlinearity, such that their ratio is close to 1:11 in this range. For increasing values of V, a second loop in the first-mode plot -centered around $V = 4$ m/s- appears, along with a corresponding resonant-like response of the (9ω) harmonic of the second mode. The pattern continues for higher velocities, with internal resonances occurring for all harmonics in increasing order. Going back to Fig. 8, the complicated loop pattern on the asymmetric branch has an identical origin, but consists of more loops due to the presence of even harmonics (2ω), (4ω) and so forth.

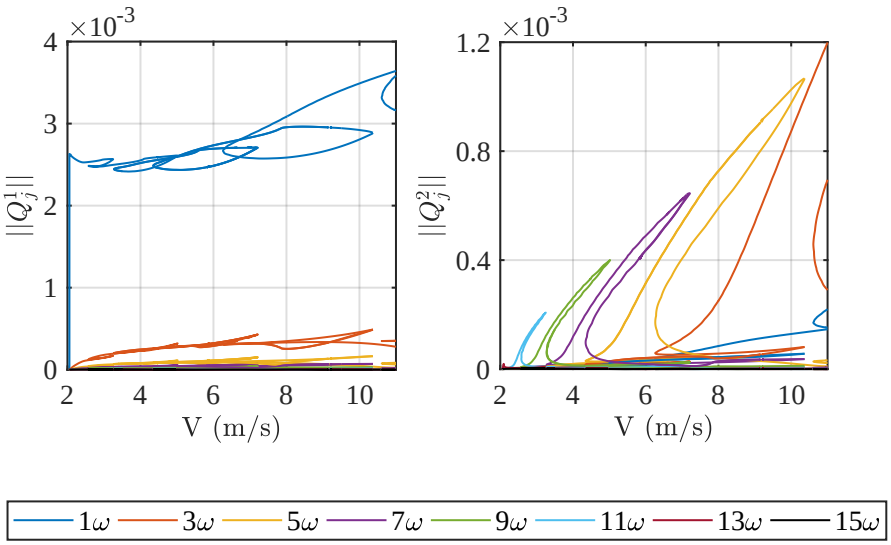

Figure 10: Evolution of harmonic amplitudes with flow velocity for the symmetric branch of two-mode model. Left: first mode ($\|Q_j^1\|$), right: second mode ($\|Q_j^2\|$). The labels ($j\omega$), for $j = 1, 3, ..., 15$, identify the contribution of the j-th harmonic to the total response for a given mode.

4.1.3. On 3-mode and further models

The pattern observed above continues with the addition of a third mode. Symmetric and asymmetric branches are represented in the $\|Q\| - V$ plane in Fig. 11 (without stability computation). Since this is a system made up of three autonomous oscillators, the solutions in time are expected to be quasi-periodic with two or three incommensurate frequencies. Qualitatively, the curves share their basic features with their two-mode predecessors (see Fig. 4.1.2 a)), although a number of additional loops within loops make their appearance. As discussed previously, this effect is more pronounced for the asymmetric branch due to a richer response spectrum.

The additional loops are a consequence of interactions between the first and the third mode, as explicitly shown for the symmetric branch in Fig. 12. Here, the total kinetic energy of each limit cycle is decomposed into modal contributions and plotted for varying V. This gives a convenient way to visualize energy transfers between the different modes. Indeed, internal resonances can be readily identified by noting the coincidence of first-mode loops and higher-mode energy peaks, a clear signature of energy transfer. Considering the third mode in particular, the first noticeable resonance corresponds to the (43ω) harmonic in the vicinity of $V = 2.9$ m/s. Internal resonances between the first and third mode become more prominent as flow velocity increases, and they always happen within a resonance peak of the second mode. Energy can be seen to cascade from the first mode to the second, then to the third, and so on. This pattern of indeed extrapolates extrapolates with the addition of further modes but, from the fourth mode onwards, the associated modal displacements are negligibly small for practically all the velocity ranges considered in our example.

4.2. Heat-exchanger arc

A more realistic configuration is now considered, as shown in Fig 13. The U-like structure has its legs pinned at a number of locations by support plates, while the uppermost arc is free but surrounded by 12 Anti-Vibration Bars (AVBs). Six of these are disposed on each side of the tube, allowing for six symmetrical, bilateral contact points with gap size $g_k = 0.24$ *mm*. Within the hydraulic circuit of a steam generator, high-temperature pressurised water flows from the hot to the cold leg of the tube, exchanging heat with the surrounding fluid along its path. Temperature and density gradients thus generate a flow of the latter in the direction x_2. This cross-flow excitation on the arc induces vibrations of the structure in the direction x_3, normal to the plane (x_1, x_2), through fluid-elastic instability, for maximum flow velocities exceeding a critical value.

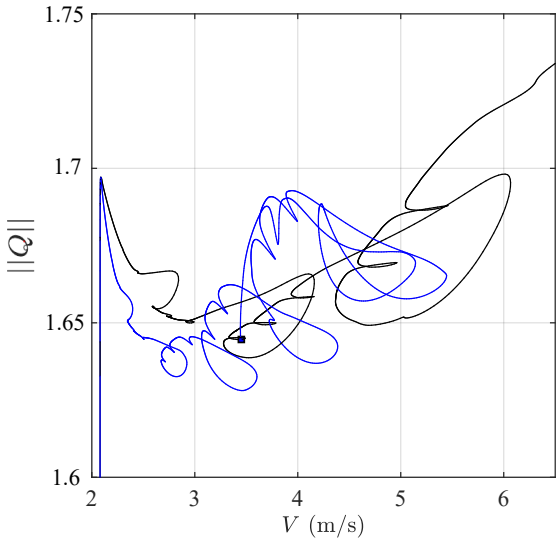

Figure 11: Continuation of periodic solutions for three-mode model. Black: symmetric branch; blue: asymmetric branch. ■: BP

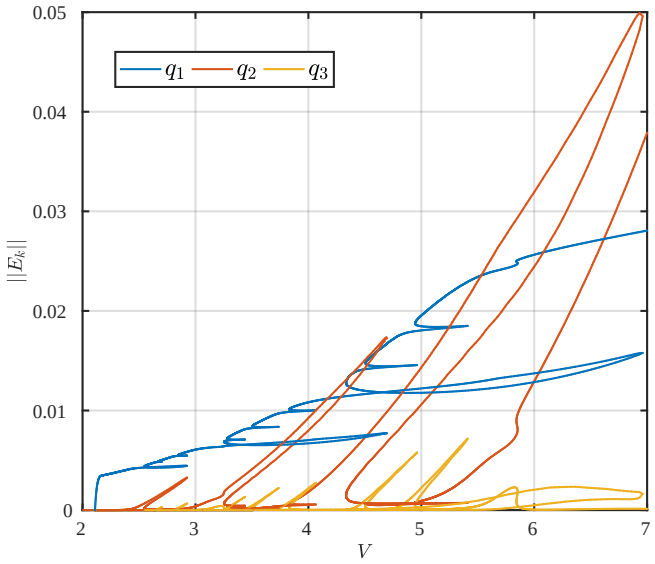

Figure 12: Modal kinetic energy for the symmetric branch of three-mode cantilever beam model. A series of energy transfers due to internal resonance between modes is observed as one travels along the branch while increasing V.

4.2.1. System description

As in the previous case study, a finite-element representation of the system described above was set up in CAST3M using linear pipe elements. A total of 310 three-dimensional elements was used, thus yielding 1860 degrees of freedom. The main characteristics of the model are summarized in Table 3.

Rather than considering uniform spatial distributions of transverse velocity and fluid density, as in the previous example, here we use thermo-hydraulic data representative of that expected to be encountered in an actual steam generator. Specifically, the distributions shown in Fig. 14 are used, which were obtained by full thermo-hydraulic simulations and first presented in [19]. In reality, the tubes are subjected to a two-phase flow consisting of liquid

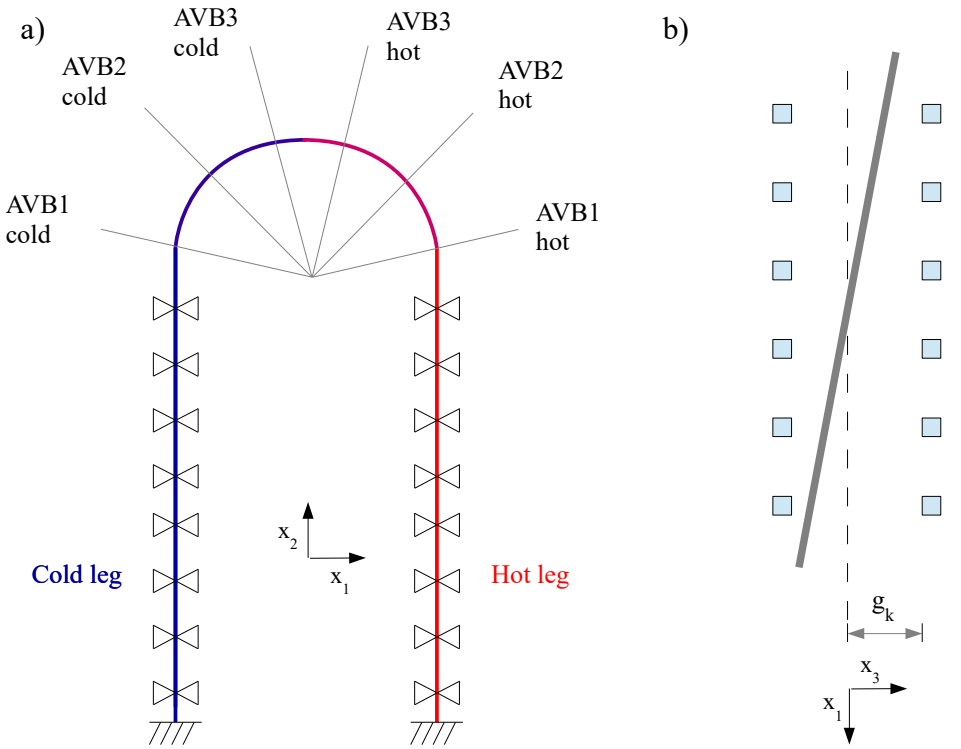

Figure 13: Heat exchanger tube. a) Frontal view, b) top view.

Radius (m)	1.577
Leg height	9.915
Number of tube support plates	9
Distance between adjacent support plates (m)	1.074
Angle from apex of AVBs (∘)	76/48/20
Tube diameter (mm)	19.05
Tube thickness (mm)	1.09
Tube density (kg.m^{-3})	8320
Nominal gap (mm)	±0.024
Impact stiffness (N/m)	4.10^5
Impact damping (Ns/m)	200
Tube density (kg.m^{-3})	8320

Table 3: Heat-exchanger tube and AVB characteristics.

water and steam. For the purposes of the present work, the flow is homogenized, and so the distributions presented correspond to those for the equivalent one-phase flow. As these distributions represent the non-fluctuating (mean) components of the respective fields, it is reasonable to assume that their shapes are invariant and scalable by ($V \equiv V_{max}, \bar{\rho}_f$) The former is used hereafter as the continuation parameter.

For the following continuation analyses, the full model was reduced by projection onto the eigenbasis of the tube in stagnant fluid and in open-gap condition. The mass matrix thus includes a contribution from the presence of fluid. It should be noted that, while the system is geometrically symmetric, the same is not true for its mode shapes. This is a consequence of the non-uniform and non-symmetric spatial distribution of equivalent density. Table 4 groups the modal properties of the first 5 out-of-plane (OP) modes. A noteworthy feature is the frequency ratio of modes 1 and

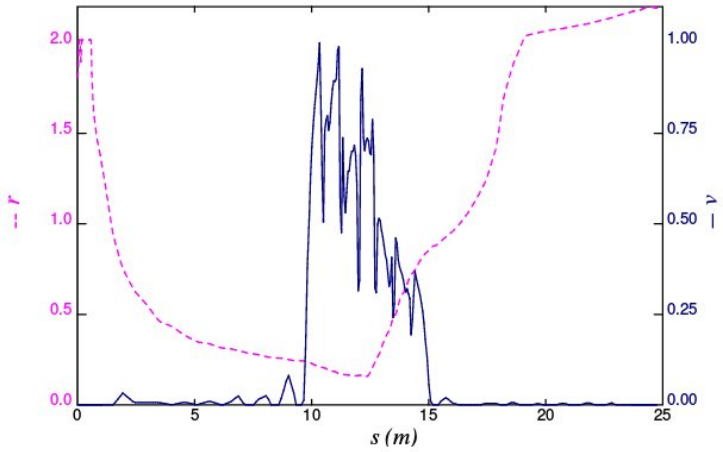

Figure 14: Distribution of normalized density r and transverse velocity ν along the tube's abscissa, s, from [19].

2, which is close to $1/3$ and can thus potentially lead to internal resonance.

Mode	1	2	3	4	5
Frequency (non-dimensional)	1.0	2.9984	6.4630	11.3844	17.0094
Mass (kg)	1.5306	1.7832	1.7315	1.8251	3.1440

Table 4: Modal properties for the U-tube model.

For all calculations presented, a 50-harmonic Fourier approximation was used, with a $N_s = 10^{11}$-point sampling. As with the previous system, $\eta = 5 \cdot 10^{-5}$. The results include phase-space diagrams of motion at the six contact points along the tube, which are identified by different colours according to the diagram shown in Fig. 15.

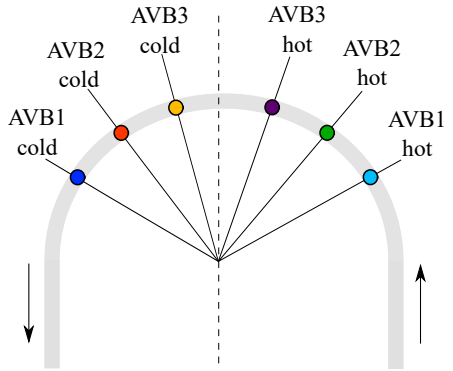

Figure 15: U-tube: colour-coding for identification of tube motions.

4.2.2. Results for 1 OP mode

The curve shown in Fig. 16 represents the evolution of Fourier coefficient amplitude for the one-mode model. All of the solutions are stable and homothetic to the regime depicted in Fig. 17 a) for $V = 5$ m/s, in which at all contact points follow a similar trajectory in phase space. The effect of impact damping is clearly seen in Fig. 17 b), obtained at the same flow velocity.

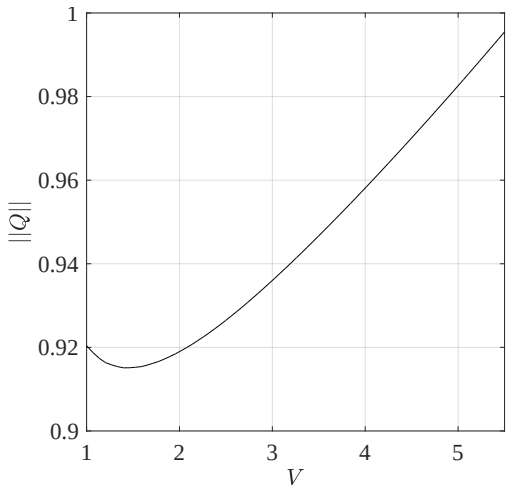

Figure 16: U-tube: Continuation for a one-OP-mode model.

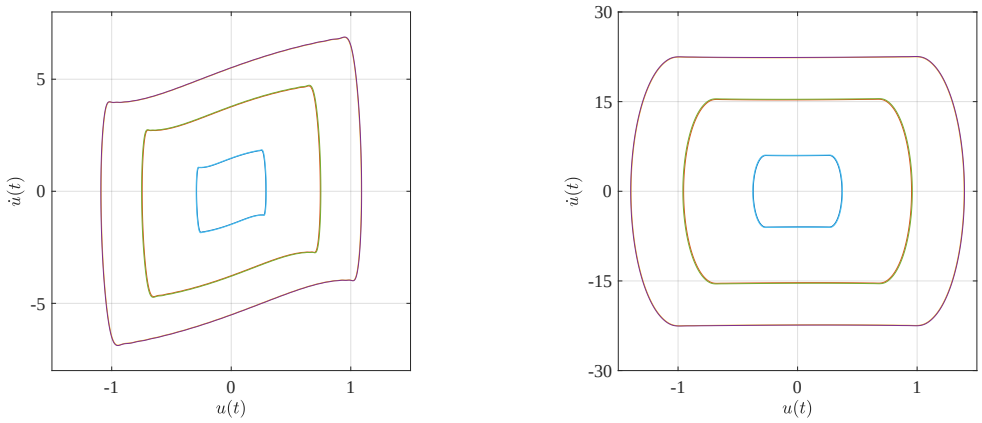

a) $c_c = 200$ b) $c_c = 0$

Figure 17: Stable regime at $V = 5$m/s for 1-mode model, considering two different values of impact damping c_c.

4.2.3. Results for 2 OP modes

When a second OP mode is included, continuation reveals the response curves of Fig. 18. The lower branch coincides exactly with the 1-mode response, but is mostly unstable. At $V = 2$ m/s, a new branch seems to bifurcate from the first. However, a closer look reveals two disjoint curves, as evidenced in Fig. 19. Regimes belonging to this curves show an increasing contribution of the second mode, which goes from virtually non-responsive on the lower branch to dominant on the upper one. Moreover, two regimes at same norm are mirrored images of each other. Hence, this behaviour is perfectly analogous to the transition branches between two and one-sided asymmetrical impacts of Sect. 4.1 with the exception that it is the Fourier coefficients of the second mode, and not those of even harmonics, that become non-zero. The fact that the branches are separated rather than overlapping and connected at a BP is a consequence of the non-uniform density distribution, which perturbs the system in a symmetry-breaking way and leads to an imperfect bifurcation.

The regimes obtained at the points A,B,C on the upper branches in Fig. 18, respectively corresponding to $V = 2.5, 3.5, 5$ m/s, are explored next. For completeness, the same is done for the dynamics at the low-velocity point D, $V = 1$ m/s. For ease of identification, the names *left branch* and *right branch* are used to refer to the branches starting at values lesser and greater than $V = 2$ m/s on Fig. (19), respectively. The transverse displacements at contact points

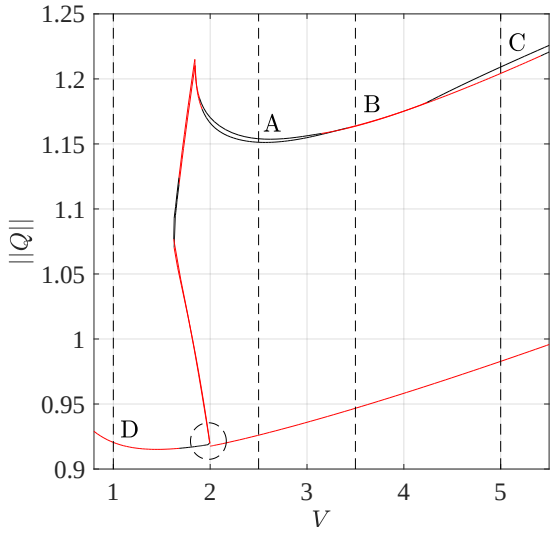

Figure 18: U-tube: Continuation for two-OP-mode model.

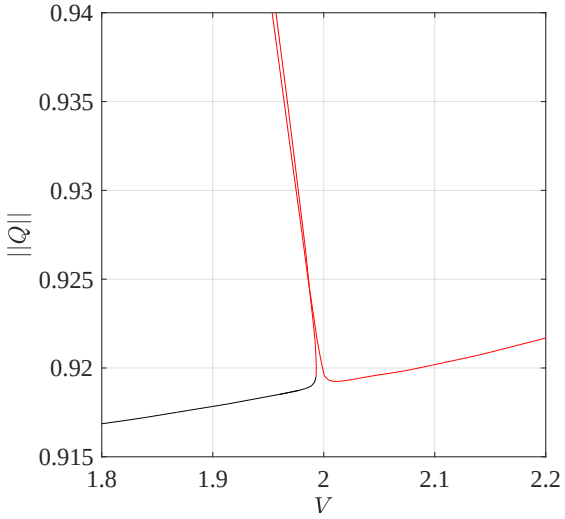

Figure 19: Close-up on the imperfect bifurcation.

are labelled $u(t)$.

*Point **A***

. The qualitative similarity of the cycles on both branches is evident from Fig. (20). Indeed, besides small differences that are a consequence of system asymmetry, the same six phase-space trajectories are observed in both images. However, the roles of points symmetrical with respect to the dotted line in Fig. 15 is reversed. This results directly from having different signs in the leading (first-harmonic) Fourier coefficient of the second mode. More precisely, for the right-branch cycle: $(Q^1_{c1}, Q^2_{c1}, Q^1_{s1}, Q^2_{s1}) = (0.9527, -0.0028, -0.1135, -0.6344)$ whereas $(Q^1_{c1}, Q^2_{c1}, Q^1_{s1}, Q^2_{s1}) = (0.9537, 0.0046, -0.1320, 0.6241)$ for its left-branch analogue.

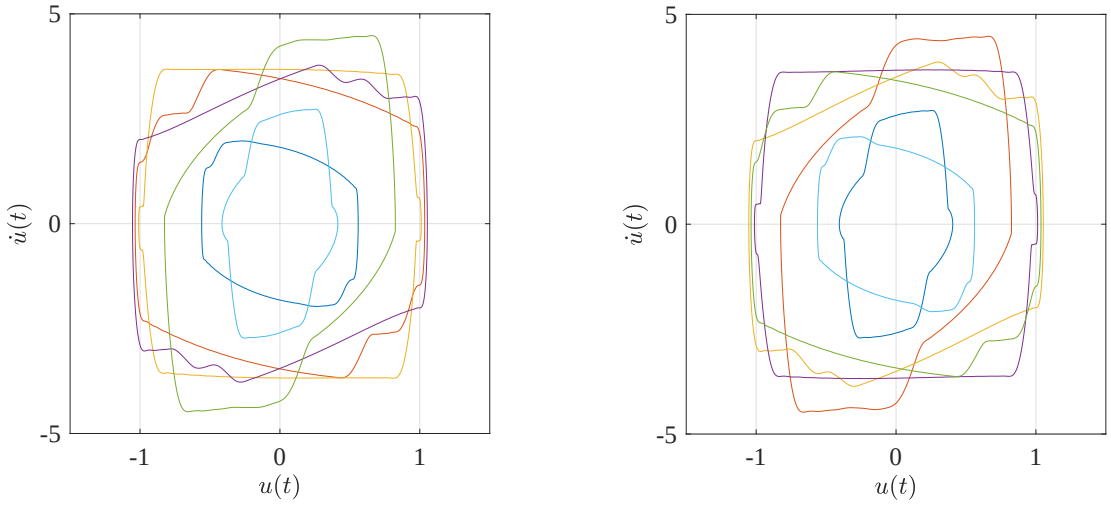

a) Right branch.

b) Left branch.

Figure 20: Coexisting stable cycles at point labelled **A** in Fig. 18, with $V = 2.5$ m/s.

*Point **B***
. Fig. 21 shows the same qualitative features as its predecessor, but in this case the cycles on both branches are unstable.

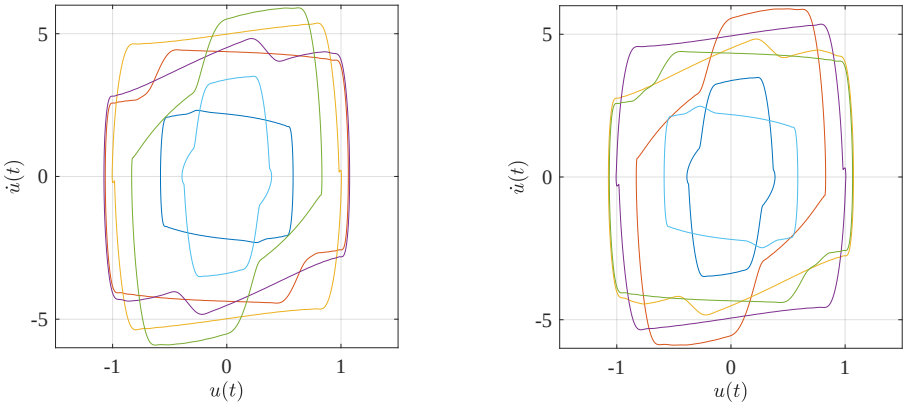

a) Right branch. b) Left branch.

Figure 21: Coexisting unstable cycles at point labelled **B** in Fig. 18, with $V = 3.5$ m/s.

The Floquet exponents around this zone indicate loss of stability through 0, i.e. a static bifurcation akin to a BP, as exemplified in Fig. 22 for the right branch[2]. However, the HBM was not able to localize the corresponding bifurcations, nor to find any periodic solutions beside the ones on the unstable branches. This hints at a transition to

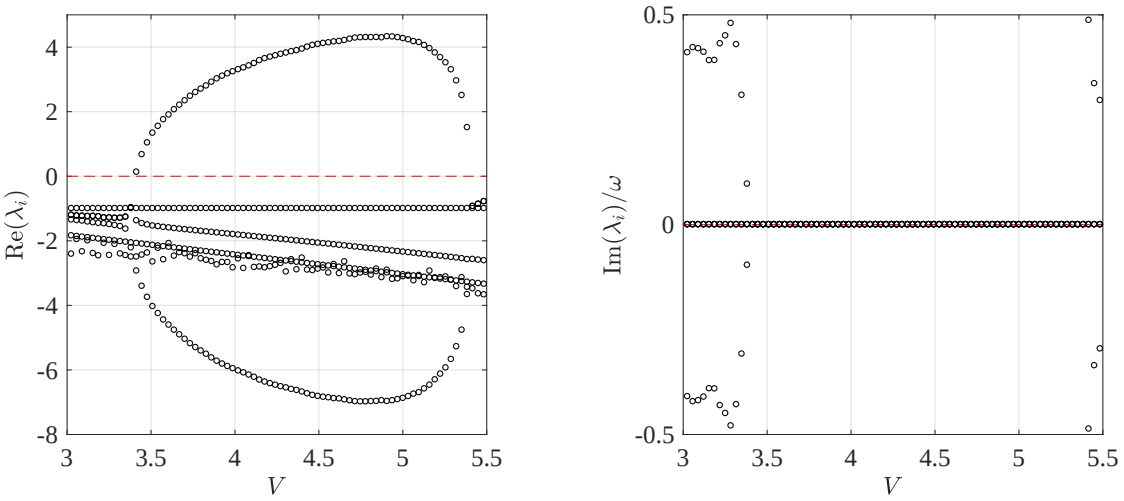

a) Real part. b) Imaginary part.

Figure 22: Floquet exponents of right branch as a function of V.

an aperiodic regime which is not quasi-periodic either, thus probably chaotic. This hypothesis seems to be supported by the time-histories and phase-space diagram depicted in Fig. 23, obtained by time integration.

The transition from a dynamically divergent, linear regime to a bounded, nonlinear one is evident. Once contacts start (when $q_1(t) = 1$), a chaotic-looking transient motion ensues. Nevertheless, long-time integration over a 1000

[2]The same behaviour is exhibited by the left branch.

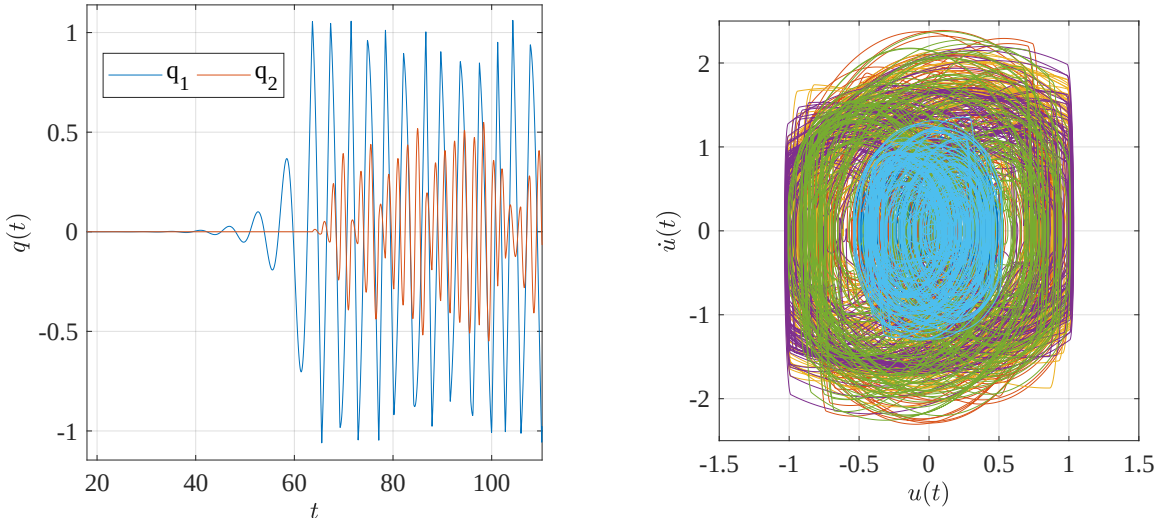

a) Modal displacements. b) Physical displacements.

Figure 23: Aperiodic regime at V = 3.5 m/s.

time-unit interval shows that this regime does not stabilize to a limit cycle. Further evidence is provided by the corresponding Power Spectral Density (PSD) diagrams, Fig. 24, which show a broadband spectrum. It should ne noted that the dominant non-dimensional frequency of the first-mode PSD (f = 0.2875), marked by a dotted line in Fig. 24 a), corresponds approximately to one third of the HBM-predicted unstable cycle frequency. A detailed investigation of the transition to chaos, which likely happens through one of the typical routes such as period-doubling or torus bifurcation cascades, is not sought in the context of this paper.

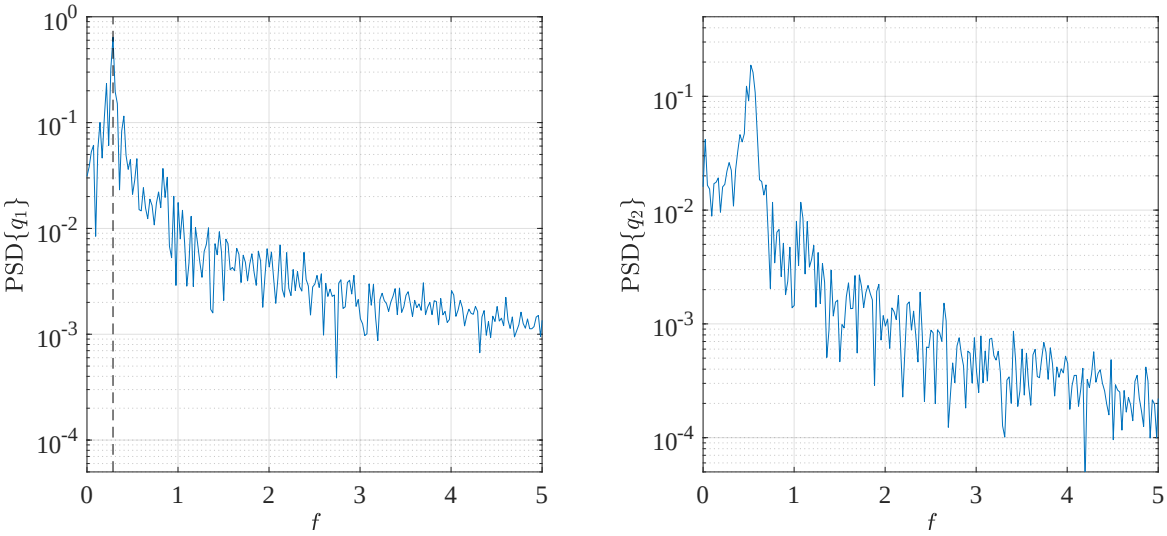

a) First mode, q_1. b) Second mode, q_2.

Figure 24: PSD of modal displacements at V = 3.5 m/s.

*Point **C***

. At this point, one branch is stable and the other is not.

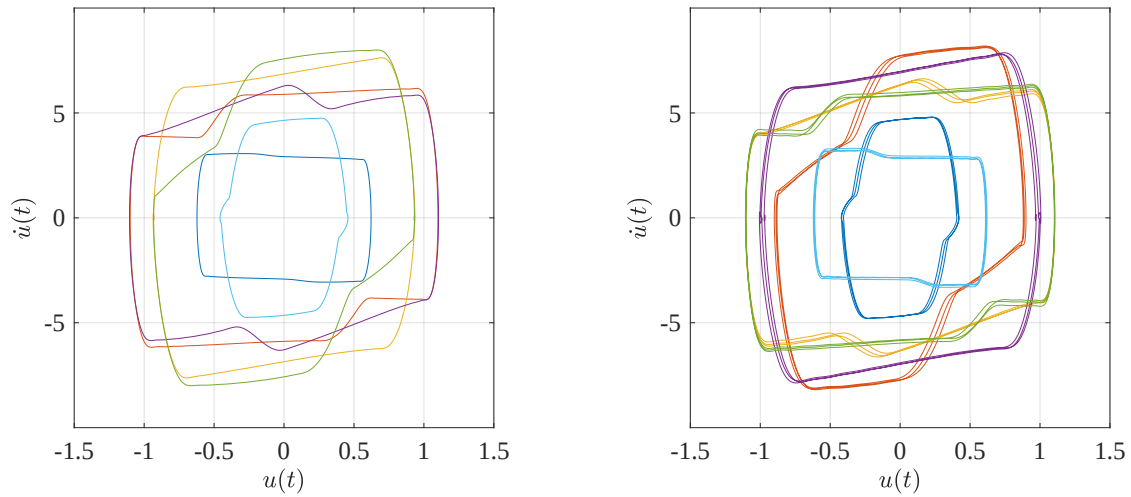

a) Right branch, T-periodic.

b) Isolated branch, 3T-periodic.

Figure 25: Stable cycles at point **C**, V = 5 m/s.

Inspired by the closing remark of last paragraph, a Fourier basis including 3T-periodic sub-harmonics was employed. In this manner, the HBM successfully captured a stable cycle with triple period in coexistence with the branches depicted in Fig. 18. Fig. 25 shows phase-space representations of stable regimes. The same trend as before, i.e. the fact that both regimes are mutually antisymmetric, is observed here, with one of them additionally being sub-harmonic.

In [19], the authors report a quasi-periodic cycle which is close to being 3T-periodic. Nevertheless, a verification through time integration yields only the stable cycles depicted in Fig. 25. Among the reasons that could explain this discrepancy in results, two of them seem most likely: the inclusion of in-plane modes in the aforementioned paper (which are absent from the present model, for HBM as well as for time-integration), or quasi-periodicity being a numerical artifice introduced by the specific integrator.

5. Conclusions

In this paper, a methodology for using numerical continuation and bifurcation analysis to study fluid-elastically-unstable tube array vibrations was presented. A frequency-domain formulation of fluid-elastic coupling forces and the stability of the computed cycles were proposed. This led to a thorough analysis of two example systems whose phenomenology is analogous to industrial steam-generator tube vibrations. In this manner, the robustness of the algorithms was showcased, while uncovering the rich dynamics associated with the nonlinear oscillation regimes. In particular, the effect of truncation in reduced-order models for the tube dynamics was seen to have a dramatic effect in continuation results, while also showing presenting visible and interpretable patterns. Moreover, it was shown that the regularization coefficient for impact forces is of prime importance for simultaneously achieving good convergence and realistic results. This opens interesting questions for further work, such as: how many linear modes must the approximation include to achieve convergence, in the sense of reproducing experimental results? For the U-tube system, how is the dynamics modified through the inclusion of in-plane modes? Is there an optimal choice for a reduction basis, and if so: how are fluid-elastic forces expressed with it? Likewise, predicting the wandering between regimes given a determined turbulence spectrum would be worthwhile for wear calculations, as would be a practical method to estimate the basins of attraction for coexisting regimes.

Appendix A. Eigenvector for the trivial zero exponent

Letting $\lambda = 0$ in Eq. (30) and writing $\boldsymbol{\phi}_0 = \left[\boldsymbol{\phi}_q^T, \boldsymbol{\phi}_v^T, \boldsymbol{\phi}_1^T, \ldots, \boldsymbol{\phi}_{n_e}^T\right]^T$, it follows immediately from the expansion of the matrix-vector product that: $\boldsymbol{\phi}_v = \omega(\nabla \otimes \mathbf{I}_n)\boldsymbol{\phi}_q$. Similarly, $\forall j = 1, ..., n_e$:

$$\boldsymbol{\phi}_j = \mathbf{S}_j(\omega)\boldsymbol{\phi}_q$$

Introducing these expressions into the second row of Eq. (30), we find that $\boldsymbol{\phi}_q$ belongs to the null-space of matrix $\mathbf{R}_\mathbf{Q}$, i.e.:

$$\mathbf{R}_\mathbf{Q}\boldsymbol{\phi}_q = \mathbf{0} \tag{A.1}$$

The singularity of $\mathbf{R}_\mathbf{Q}$ comes from the fact that autonomous systems are invariant with respect to translations in time, i.e. the initial phase is free: if $\mathbf{q}(t)$ is a solution to the equations of motion, then $\mathbf{q}(t + \delta t)$ is as well, $\forall \delta t \in \mathbb{R}$. The Fourier expansion of the latter can be expressed in two equivalent ways, either in terms of the coefficients associated with zero phase shift, $\mathbf{Q}$, or by considering a new vector $\mathbf{Q}_{\delta t}$:

$$\mathbf{q}(t + \delta t) = [\mathbb{F}_H(\omega(t + \delta t)) \otimes \mathbf{I}_n]\,\mathbf{Q} = [\mathbb{F}_H(\omega t) \otimes \mathbf{I}_n]\,\mathbf{Q}_{\delta t} \tag{A.2}$$

This relation simply states the fact that a phase shift equates to a rotation of the harmonic coefficients by an angle δt in the frequency domain, while their amplitudes are kept constant. Indeed, by using trigonometric identities: $\mathbb{F}_H(\omega(t + \delta t)) = \mathbb{F}_H(\omega t)\mathbf{G}(\omega\delta t)$, where :

$$\mathbf{G}(\omega\delta t) = \mathrm{diag}\left(1, \begin{bmatrix} \cos(\omega\delta t) & \sin(\omega\delta t) \\ -\sin(\omega\delta t) & \cos(\omega\delta t) \end{bmatrix}, ..., \begin{bmatrix} \cos(H\omega\delta t) & \sin(H\omega\delta t) \\ -\sin(H\omega\delta t) & \cos(H\omega\delta t) \end{bmatrix}\right)$$

$$\implies \mathbf{Q}_{\delta t} = (\mathbf{G}(\omega\delta t) \otimes \mathbf{I}_n)\mathbf{Q} \tag{A.3}$$

Now, if $\mathbf{Q}$ satisfies dynamical equilibrium, the invariance property implies that $\mathbf{Q}_{\delta t}$ must do the same for any δt. Hence: $\mathbf{R}(\mathbf{Q}_{\delta t}) = \mathbf{0}$ and, moreover:

$$\frac{d\mathbf{R}(\mathbf{Q}_{\delta t})}{d\phi_0} = \frac{\partial \mathbf{R}}{\partial \delta t} + \mathbf{R}_\mathbf{Q}(\mathbf{Q}_{\delta t})\frac{d\mathbf{Q}_{\delta t}}{d\delta t} = \omega\mathbf{R}_\mathbf{Q}(\mathbf{Q}_{\delta t})(\mathbf{G}(\omega\delta t)\nabla \otimes \mathbf{I}_n)\mathbf{Q} = \mathbf{0}$$
$$\implies \mathbf{R}_\mathbf{Q}(\mathbf{Q}_{\delta t})(\nabla \otimes \mathbf{I}_n)\mathbf{Q}_{\delta t} = \mathbf{0} \tag{A.4}$$

Hence, regardless of the chosen initial phase, the eigenvector associated to the singular value is given by Eq. (A.4). Furthermore, by identifying Eqs. (A.1) and (A.4), it is clear that $\boldsymbol{\phi}_\eta = (\nabla \otimes \mathbf{I}_n)\mathbf{Q}$. With this in mind, the eigenvector $\boldsymbol{\phi}_0$ can be readily constructed and so the trivial zero is shifted away to a new value $\epsilon < 0$ during bifurcation analysis, while the rest of the spectrum remains unchanged. In other words, stability evaluation is given by the eigenvalues of the matrix:

$$\tilde{\mathbb{H}} = \mathbb{H} - \epsilon\frac{\boldsymbol{\phi}_\mathbf{0}\boldsymbol{\phi}_0^T}{\|\boldsymbol{\phi}_0\|^2} \tag{A.5}$$

References

[1] F. Axisa, J. Antunes, Modelling of Mechanical Systems: Fluid-Structure Interaction, Butterworth-Heinemann, 2006.

[2] H. J. Connors, Flow-induced vibration and wear of steam generator tubes, Nuclear Technology 55 (2) (1981) 311–331. doi:10.13182/nt55-311.

[3] M. Païdoussis, Fluidelastic vibration of cylinder arrays in axial and cross flow: State of the art, Journal of Sound and Vibration 76 (3) (1981) 329–360. doi:10.1016/0022-460x(81)90516-2.

[4] M. Païdoussis, A review of flow-induced vibrations in reactors and reactor components, Nuclear Engineering and Design 74 (1) (1983) 31–60. doi:10.1016/0029-5493(83)90138-3.

[5] M. P. Païdoussis, Flow-induced instabilities of cylindrical structures, Applied Mechanics Reviews 40 (2) (1987) 163–175. doi:10.1115/1.3149530.

[6] M. Païdoussis, Real-life experiences with flow-induced vibration, Journal of Fluids and Structures 22 (6-7) (2006) 741–755. doi:10.1016/j.jfluidstructs.2006.04.002.

[7] S. sheng Chen, Vibration of nuclear fuel bundles, Nuclear Engineering and Design 35 (3) (1975) 399–422. doi:10.1016/0029-5493(75)90071-0.

[8] S. Chen, Guidelines for the instability flow velocity of tube arrays in crossflow, Journal of Sound and Vibration 93 (3) (1984) 439–455. doi:10.1016/0022-460x(84)90340-7.

[9] M. Pettigrew, L. Carlucci, C. Taylor, N. Fisher, Flow-induced vibration and related technologies in nuclear components, Nuclear Engineering and Design 131 (1) (1991) 81–100. doi:10.1016/0029-5493(91)90319-d.

[10] S. Price, A review of theoretical models for fluidelastic instability of cylinder arrays in cross-flow, Journal of Fluids and Structures 9 (5) (1995) 463–518. doi:10.1006/jfls.1995.1028.

[11] H. Gelbe, M. Jahr, K. Schröder, Flow-induced vibrations in heat exchanger tube bundles, Chemical Engineering and Processing: Process Intensification 34 (3) (1995) 289–298. doi:10.1016/0255-2701(94)04016-8.

[12] T. Sarpkaya, A critical review of the intrinsic nature of VIV, in: IUTAM Symposium on Integrated Modeling of Fully Coupled Fluid Structure Interactions Using Analysis, Computations and Experiments, Springer Netherlands, 2003, pp. 159–161. doi:10.1007/978-94-007-0995-9\textunderscore10.

[13] R. Gibert, Vibrations des structures. Interactions avec les fluides. Sources d'excitation aleatoires, Ed. Eyrolles, 1988.

[14] M. P. Païdoussis, S. J. Price, E. D. Langre, Fluid-Structure Interactions, Cambridge University Press, 2013.

[15] N. Sun, R. jia Cheng, Y. nan Zhang, B. qing Liu, B. Sunden, Design guidelines for fluid-elastic instability of tube bundles subjected to two-phase cross flow, Journal of Zhejiang University-SCIENCE A 20 (8) (2019) 577–589. doi:10.1631/jzus.a1900129.

[16] C. E. Taylor, M. J. Pettigrew, A design guideline for random excitation forces due to two-phase cross flow in tube bundles, Journal of Pressure Vessel Technology 142 (6) (aug 2020). doi:10.1115/1.4047496.

[17] P. P., D. X., B. L., J. Antunes, An improvement to the quasi-steady model with application to cross-flow-induced vibration of tube arrays, Journal of Fluids ans Structures 86 (2019) 156–169. doi:10.1016/j.jfluidstructs.2019.02.001.

[18] L. Borsoi, P. Piteau, X. Delaune, J. Antunes, Competition between turbulence and fluid-elastic forces in the response of a loosely supported tube under cross-flow, Procedia Engineering 199 (Supplement C) (2017) 1282 – 1289, X International Conference on Structural Dynamics, EURODYN 2017. doi:https://doi.org/10.1016/j.proeng.2017.09.310.
URL http://www.sciencedirect.com/science/article/pii/S1877705817337943

[19] B. Prabel, P. Piteau, L. Borsoi, J. Antunes, Non-linear vibration of heat exchanger tubes subjected to fluidelastic forces, in: Proceedings of 9th International Symposium on Fluid-Structure Interactions, Flow-Sound Interactions, Flow-Induced Vibration & Noise., 2018.

[20] J. Lai, L. Sun, P. Li, Two-phase flow-induced instability and nonlinear dynamics of a single tube in tube bundles in the transverse direction, European Journal of Mechanics - A/Solids 78 (2019) 103858. doi:10.1016/j.euromechsol.2019.103858.

[21] S. J. Price, M. P. Paidoussis, A single-flexible-cylinder analysis for the fluidelastic instability of an array of flexible cylinders in cross-flow, Journal of Fluids Engineering 108 (2) (1986) 193–199. doi:10.1115/1.3242562.

[22] J. Sieber, K. Engelborghs, T. Luzyanina, G. Samaey, D. Roose, DDE-BIFTOOL Manual — Bifurcation analysis of delay differential equations. sourceforge.net/projects/ddebiftool and sourceforge.net/p/ddebiftool/git/ci/master/tree/ddebiftool_coco.

[23] R. Szalai, Knut: A continuation and bifurcation software for delay-differential equations. https://rs1909.github.io/knut/. Accessed: 2024-01-24.

[24] Z. Ahsan, H. Dankowicz, M. Li, J. Sieber, Methods of continuation and their implementation in the coco software platform with application to delay differential equations, Nonlinear Dyn 107 (2022) 3181–3243. doi:10.1007/s11071-021-06841-1.

[25] R. Alcorta, S. Baguet, B. Prabel, P. Piteau, G. Jacquet-Richardet, Period doubling bifurcation analysis and isolated sub-harmonic resonances in an oscillator with asymmetric clearances, Nonlinear Dynamics 98 (4) (2019) 2939–2960. doi:10.1007/s11071-019-05245-6.

[26] C. Grenat, S. Baguet, C.-H. Lamarque, R. Dufour, A multi-parametric recursive continuation method for nonlinear dynamical systems, Mechanical Systems and Signal Processing 127 (2019) 276–289. doi:10.1016/j.ymssp.2019.03.011.

[27] L. Guillot, B. Cochelin, C. Vergez, A taylor series-based continuation method for solutions of dynamical systems, Nonlinear Dynamics 98 (4) (2019) 2827–2845. doi:10.1007/s11071-019-04989-5.

[28] O. Deblecker, J. Lobry, A new efficient technique for harmonic-balance finite-element analysis of saturated electromagnetic devices, IEEE Trans. on Magn. 42 (4) (2006) 535–538.

[29] D. Detroux, L. Renson, L. Masset, G. Kerschen, The harmonic balance method for bifurcation analysis of large-scale nonlinear mechanical systems, in: 22ème Congrès Français de Mécanique, 2015.

[30] J. Blahoš, A. Vizzaccaro, L. Salles, F. Haddad, Parallel harmonic balance method for analysis of nonlinear dynamical systems, in: Proceedings of ASME Turbo Expo 2020 Turbomachinery Technical Conference and Exposition GT2020, 2020. doi:10.1115/GT2020-15392.

[31] J. Antunes, F. Axisa, M. A. Vento, Experiments on tube/support interaction with feedback-controlled instability, Journal of Pressure Vessel Technology 114 (1) (1992) 23–32. doi:10.1115/1.2929008.

[32] B.H.K., L. Gong, Y. Wong, Analysis and computation of nonlinear dynamic response of a two-degree-of-freedom system and its application in aeroelasticity, Journal of Fluids and Structures 11 (3) (1997) 225–246. doi:https://doi.org/10.1006/jfls.1996.0075.

[33] K. Chung, C. Chan, B. Lee, Bifurcation analysis of a two-degree-of-freedom aeroelastic system with freeplay structural nonlinearity by a perturbation-incremental method, Journal of Sound and Vibration 299 (3) (2007) 520–539. doi:10.1016/j.jsv.2006.06.059.

[34] G. Dimitriadis, Shooting-based complete bifurcation prediction for aeroelastic systems with freeplay, Journal of Aircraft 48 (6) (2011) 1864–1877. doi:10.2514/1.c031139.

[35] J. Antunes, F. Axisa, B. Beaufils, D. Guilbaud, Coulomb friction modelling in numerical simulations of vibration and wear work rate of multispan tube bundles, Journal of Fluids and Structures 4 (3) (1990) 287–304. doi:10.1016/s0889-9746(05)80016-7.

[36] K. H. Hunt, F. R. E. Crossley, Coefficient of restitution interpreted as damping in vibroimpact, Journal of Applied Mechanics 42 (2) (1975) 440–445. doi:10.1115/1.3423596.

[37] T. Kim, T. Rook, R. Singh, Effect of smoothening functions on the frequency response of an oscillator with clearance non-linearity, Journal of Sound and Vibration 263 (3) (2003) 665–678. doi:10.1016/s0022-460x(02)01469-4.

[38] B. Brogliato, Nonsmooth Mechanics, Springer-Verlag, 1999.

[39] M. P. Granger, S.; Païdoussis, An improvement to the quasi-steady model with application to cross-flow-induced vibration of tube arrays,

Journal of Fluid Mechanics 320 (1996) 163–184. doi:10.1017/S0022112096007495.
[40] H. Banks, A brief review of some approaches to hysteresis in viscoelastic polymers, Nonlinear Analysis: Theory, Methods & Applications 69 (3) (2008) 807–815. doi:10.1016/j.na.2008.02.103.
[41] G. Kiss, , B. Krauskopf, Stability implications of delay distribution for first-order and second-order systems, Discrete & Continuous Dynamical Systems - B 13 (2) (2010) 327–345. doi:10.3934/dcdsb.2010.13.327.
[42] S. A. Campbell, Time delays in neural systems, in: Understanding Complex Systems, Springer Berlin Heidelberg, 2007, pp. 65–90. doi:10.1007/978-3-540-71512-2\textunderscore2.
[43] R. Sipahi, F. M. Atay, S.-I. Niculescu, Stability of traffic flow behavior with distributed delays modeling the memory effects of the drivers, SIAM Journal on Applied Mathematics 68 (3) (2008) 738–759. doi:10.1137/060673813.
[44] H. Smith, An Introduction to Delay Differential Equations with Applications to the Life Sciences, Springer New York, 2011. doi:10.1007/978-1-4419-7646-8.
[45] P. Piteau, X. Delaune, L. Borsoi, J. Antunes, Experimental identification of the fluid-elastic coupling forces on a flexible tube within a rigid square bundle subjected to single-phase cross-flow, Journal of Fluids and Structures 86 (2019) 156–169. doi:10.1016/j.jfluidstructs.2019.02.001.
[46] J. H. Cameron, T. M. ; Griffin, An alternating frequenct/time domain method for calculating the steady-state response of nonlinear dynamic systems, Journal of Applied Mechanics, ASME 56 (1) (1989) 149–154.
[47] L. Xie, S. Baguet, B. Prabel, R. Dufour, Bifurcation tracking by harmonic balance method for performance tuning of nonlinear dynamical systems, Mechanical Systems and Signal Processing 88 (2017) 445–461. doi:10.1016/j.ymssp.2016.09.037.
[48] B. Bentvelsen, A. Lazarus, Modal and stability analysis of structures in periodic elastic states: application to the ziegler column, Nonlinear Dynamics 91 (2) (2017) 1349–1370. doi:10.1007/s11071-017-3949-4.
[49] Y. Saad, Numerical Methods for Large Eigenvalue Problems, CAMBRIDGE, 2011.
[50] Y. A. Kuznetsov, Elements of Applied Bifurcation Theory, Springer New York, 2004. doi:10.1007/978-1-4757-3978-7.
[51] A. Griewank, G. Reddien, The calculation of hopf points by a direct method, IMA Journal of Numerical Analysis 3 (3) (1983) 295–303. doi:10.1093/imanum/3.3.295.
[52] Cast3m, http://www-cast3m.cea.fr.